Ore Geology Reviews 84 (2017) 134–153

Contents lists available at ScienceDirect

Ore Geology Reviews

journal homepage: www.elsevier.com/locate/oregeo

Review

Petrography, mineralogy and geochemistry of the Late Eocene oolitic ironstones of the Jebel Ank, Southern Tunisian Atlas

Hechmi Garnit *, Salah Bouhlel

Unité de Géochimie et Géologie de l'Environnement UR11ES16, Département de Géologie, Faculté des Sciences de Tunis, Université de Tunis El Manar, 2092 Tunis, Tunisia

ARTICLE INFO

Article history:
Received 17 April 2016
Received in revised form 22 October 2016
Accepted 28 December 2016
Available online 13 January 2017

Keywords:
Geochemical characterization
Oolitic ironstone
Jebel Ank
Tunisia

ABSTRACT

The oolitic ironstones ore deposit of Jebel Ank (central Tunisia), is a simply folded stratiform ore body of about 2.5–8 m thickness located in the upper part of the epicontinental Souar Formation (Late Eocene) and is covered by the continental Segui Formation (Mio-Pliocene). The deposit contains about 20 Mt of ore with an average grade of 50% Fe. Generally, oolitic iron deposition occurs in shallow water lagoonal environments. The Jebel Ank deposit lies between two regional disconformities (Late Eocene and Miocene), and is evidence of a transitional stage at the end of regional regression before renewed transgression. The footwall of the oolitic iron ore-bearing bed consists of a fine-grained sandstone bed (10–20 cm-thick) pinching out laterally westward into green clays. The hanging wall is composed of thin-bedded limestone and clay alternations (2–3.5 m-thick).

Iron occurs in the form of cryptocrystalline goethite with limited Al-Fe substitution. The goethite contains around 48% Fe, 5% Al and up to 1.5% P. Jarosite, alunite and manganese minerals (cryptomelane, psilomelane and manjiorite) are supergene secondary minerals, probably related to descending surface fluids. These manganese minerals occur as accessory minerals with the goethite and are most abundant at the lowermost part of the succession showing varied morphologies (local cement, space filling and free centimeter sized nodules). Fe-oolites in the deposit are similar to those documented in many other oolitic ironstone deposits. The dominant Fe-oolite type (>90%) has a concentrically laminated cortex with no nucleus. The nuclei of the oolites that do have a nucleus are most commonly detrital quartz grains.

Major elements in high grade samples (Fe_2O_3 > 65%) vary within a limited range and show higher concentrations of SiO_2 (average 7.85%) and Al_2O_3 (average 5.1%), with minor TiO_2, MnO, MgO, Na_2O, K_2O, and SO_3 (less than 1%). PAAS-normalized trace elements of bulk samples and Fe-oolite generally show similar behavior, both are enriched in V, Co, Ni, Mo, As, Zn, and Y and are depleted in Cu, Rb, Zr, Nb, Ba, and Hf. Anomalous V, Cr, Ni, Zn, and REE-Y are correlated with goethite. PAAS-normalized REE-Y patterns of both bulk samples and Fe-oolite show slight HREE enrichment, positive Ce with negative Y anomalies.

The mineralogy (goethite and cryptomelane) along with the geochemistry (Si *vs.* Al; As + Cu + Mo + Pb + V + Zn *vs.* Ni + Co binary plots; Zn–Ni–Co triangular diagram, REE-Y content and patterns and Ce/Ce^* *vs.* Nd and Ce/Ce^* *vs.* Y_N/Ho_N binary plots) of the studied oolitic ironstone are congruent with a hydrogenetic type. While two possible sources of iron for Jebel Ank ironstone can be proposed: (i) submarine weathering of glauconite-rich sandstone and (ii) detrital iron from adjacent continental hinterland, the later is the more plausible source of iron, based on paleogeographic setting, the occurrence of fine sandstone underlying the iron level, occurrence of Mn-ores in the lower part of the Fe-ores succession, high phosphorous, zinc, ∑REE-Y concentrations and Y/Ho ratios, and low La/Ce ratios.

Contents

* Corresponding author.
E-mail address: garnit1hechmi@yahoo.fr (H. Garnit).

http://dx.doi.org/10.1016/j.oregeorev.2016.12.026
0169-1368/

1. Introduction

Oolitic ironstone deposits of Tertiary age are widespread in northern Europe, northern Africa and southern United States, but most are of minor dimensions (James, 1966). The Middle Eocene ironstone deposits of El Bahariya Depression (Egypt) represent the only economic oolitic ironstone along the Tertiary paleo-Tethyan shorelines in northern Africa and southern Europe (Salama et al., 2012).

Although the Jebel Ank (Mount Ank) is the only known oolitic ironstone deposit in Tunisia, it is important to point out that in northern Africa (Algeria, Egypt, Sudan and Nigeria), other Late Cretaceous-Tertiary oolitic ironstones occur in siliciclastic-carbonate sequences and are also related to manganiferous, phosphorite mineralizations and Fe-laterites (Van Houten, 1992; Petránek and Van Houten, 1997). They were particularly well developed during the Early and Middle Eocene, which reflects the paleoclimatic and paleogeographical controls on the development of this sedimentary Fe-mineralization and represent a proxy for Early Paleogene climate and sea-level changes (Salama et al., 2014).

The Jebel Ank oolitic ironstone deposit is located in central Tunisia, about 30 km south east of Gafsa city on the road joining Gafsa to El Guettar-Bou Omrane towns (Fig. 1A). It lies at the eastern side of the Tertiary phosphorites-rich Gafsa-Metlaoui basin. This area contains the giant sedimentary phosphorite deposits and the unique ironstone deposit of the Jebel Ank. The ironstone ores are stratigraphically located in the upper part of the Late Eocene succession under the discordant Mio-Pliocene series.

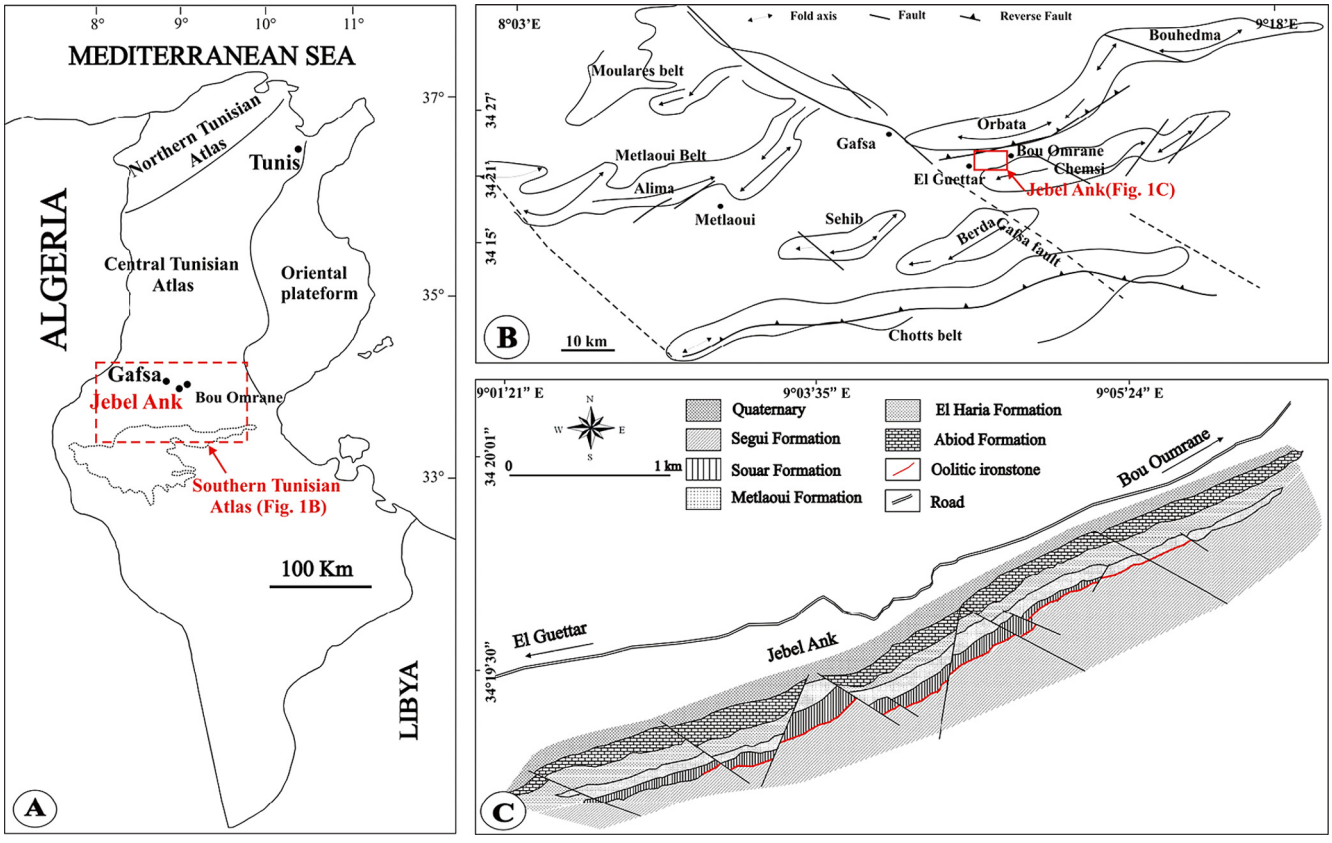

Fig. 1. (A) Simplified structural map of Tunisia showing the location of Jebel Ank. (B) Simplified structural map of the southern Atlas foreland of Tunisia (Geological map of Tunisia 1/500.000, after Ben Haj Ali et al., 1985). (C) Geological map of Jebel Ank showing the main outcrops and the lateral extension of the oolitic ironstone level (after M'hamdi, 1984).

In 1932, the concession of Jebel Ank was acquired by the Company of Phosphates of M'dhilla. During the period 1949–1960 geological surveys and mineral processing testing were undertaken. In the early 1960s, the concession was recovered by the National Office of Mines. Metallogenic investigations have revealed an apparently new economic potential. On March 2006, the concession was granted by official directive to the Jebel Jerissa Society. Finally, in 2007 the exploration license was granted to the local Mining and Steel Company. The company proceeded with a beneficiation and metallurgical testing program to define the ore grade distribution, the economic resources, and the chemical quality of the ores. The calculated, proven reserves are about 5 Mt and the probable, and possible resources are about 20 Mt with an average grade of 50% Fe.

The Jebel Ank deposit was described successively by Berthon (1922) and Gottis and Sainfeld (1952), who gave a brief geologic settings and exploitation oriented description of the deposit. Sassi (1974) gave an overview of the stratigraphy of the region and assigned an Eocene age to the Fe-mineralization.

The oolitic ironstone deposit of the Jebel Ank was first reported by Berthon (1922) to be of Middle Eocene age. Gottis and Sainfeld (1952) reported that the Jebel Ank is unique, being the only known oolitic ironstone of Tunisia. Nicolini (1967) defined the paleogeographic and sedimentological context of the deposit and discussed some similarities of the Ank oolitic Fe-ores with the Minette ironstone of the Lorraine basin in France. M'hamdi (1984) gave an overview of the mineralogy and petrography together with bulk chemical analysis and discussed the palaeogeographic control and possible Fe-sources.

Publications with detailed databases addressing the characterization and genesis of the Fe-mineralization are scarce. New insights based on field, petrographic, mineralogical and geochemical studies of the ironstone deposit are provided in this article, using techniques such as X-ray diffraction (XRD), Scanning electron microscopy and energy dispersive spectroscopy (SEM-EDS), Fourier transform infrared spectroscopy (FTIR), RAMAN spectroscopy, Inductively Coupled Plasma-Mass Spectrometry (ICP-MS) and Laser ablation ICP-MS (LA-ICP-MS). The purpose of this study is to characterize Fe-mineralization and discuss possible ore sources.

2. Geologic setting

2.1. Regional geology

The Jebel Ank deposit lies in the Southern Tunisian Atlas (Fig. 1A), which corresponds to a system of foreland fold and thrust belts bordered to the east by the NW-SE trending Gafsa fault (Zargouni, 1985). This Atlasic domain is composed of NE-SW and E-W trending folds and NW-SE trending thrusts that form the Metlaoui-Gafsa belt and the Chotts belt (Zargouni, 1985; Zouari et al., 1990; Ben Ayed, 1993; Boukadi, 1994) (Fig. 1B). The Jebel Ank area is delimited by several NE–SW to E–W structural lineaments: the Orbata and Bouhedma belts to the north and northeastern, respectively; the Jebel Chemsi and Jebel Berda to the south and southwestern, respectively (Fig. 1B). These structural lineaments mainly consist of asymmetric southeast-plunging anticlines cored by Late Cretaceous series rocks (Boukadi, 1985). This area is affected by several NW–SE and E–W trending faults.

Several geometric and kinematic models have been proposed for the Southern Tunisian Atlas folds and thrusts. They have been variously interpreted as: (i) fault propagation folding (e.g. Bensalem et al., 2010; Ahmadi et al., 2013); (ii) thick-skinned tectonics style folding involving the Paleozoic basement (Hlaiem, 1999; Zouaghi et al., 2011); (iii) NW-SE oblique ramps and tear faults (Said et al., 2011) with mixed tectonic style and deep-seated basement faults, shallower decollements within sedimentary cover, and salt diapirism (Gharbi et al., 2015).

The folds are composed of Cretaceous and Cenozoic series. Subsurface data showed that some anticline cores and some faults are injected by Triassic salt diapirs (Hlaiem, 1999; Zouaghi et al., 2005). The Cretaceous series are composed of carbonate rocks, shales, marls, sandstones, and evaporites. The Late Cretaceous series are composed of carbonates and are overlain by the Paleocene marls. The Early to Middle Paleocene series are characterized by marls and marly limestone, alternations of bioclastic carbonates, marls, and evaporites indicative of restricted environments. During the Late Paleocene-Early Eocene, clays, carbonates, chert and phosphorites were deposited. From the Middle to Late Eocene, massive gypsum beds intercalated with claystone were deposited. The Late Eocene marked the end of marine sedimentation.

The Cretaceous-Cenozoic transition is marked by regional unconformities, gaps, and condensed series (Burollet, 1956; Zargouni et al., 1985; Zouari et al., 1990; Boukadi, 1994; Zouaghi et al., 2005). The marine Cretaceous-Eocene series are mostly covered by discordant Neogene continental formations made of detrital alluvial and fluvial deposits.

Outcrops and subsurface geology attest that the region was subjected to more than one phase of tectonic activity, mainly a N-S extensional regime from the Triassic to Late Cretaceous and a NE-SW and NW-SE compressive regime from the Eocene to the present (Bouaziz et al., 2002). These periods are marked by principal tectonic phases of compression trending NW-SE to N-S, which are related to the mechanisms of collision between the African and Eurasian plates (e.g. Dercourt et al., 1986).

2.2. Local geology

The Jebel Ank is located within the E-W-trending belts along the eastern side of the southern Atlas, approximately 30 km southeastern of the Gafsa city and 2 km south of the Bou Omrane town (Fig. 1B). The deposit is located on the eastern border of the phosphorites-rich Gafsa-Metaloui basin. In this border area, uneconomic stratiform phosphorites are exposed in two main zones: along the southern flank of the anticline of Orbata at Jebel Hamadi and Jebel Ank and along the northern flank and the western periclinal closure of the anticline of Jebel Chemsi (Fig. 1B). At Jebel Ank, the phosphatic series is correlated with the phosphorite of Chouabine Formation of the Gafsa-Metlaoui basin.

The asymmetric synclinal structure of Jebel Ank is a part of an extended syncline structure trending WSW-ENE, about 20 km long stretching between Jebel Orbata to the north and Jebel Chemsi to the south (Fig. 1B). Jebel Ank lies between latitudes 34°20′18″–34°19′37″N and longitudes 09°01′21″–09°06′04″E (Fig. 1C).

The synclinal structure is formed from the base and upward by the Campanian limestones, the Paleocene (clays and marls), the Eocene carbonates, and the Late Mio-Pliocene conglomerates, marls, sands and red clays. Two major NW-SE trending normal faults divided the structure into three blocks (Fig. 1C). The dips of rock units along the northern and southern flanks of Jebel Ank vary, with subvertical layers of the northern flank related to E-W trending faults (Fig. 2A).

In the Jebel Ank area, the stratigraphic series range from the Campanian to Pliocene successions, which are subdivided into five main formations (Abiod, El Haria, Metlaoui, Souar, and Segui formations) (Fig. 2A). The Abiod Formation (Campanian-Early Maastrichtian) is composed mainly of carbonates (Fig. 2A). The El Haria Formation (Late Maastrichtian-Early Paleocene), which rests disconformably on the Abiod Formation, is composed of about 60 m-thick grey-olive green clays (smectite and kaolinite at the

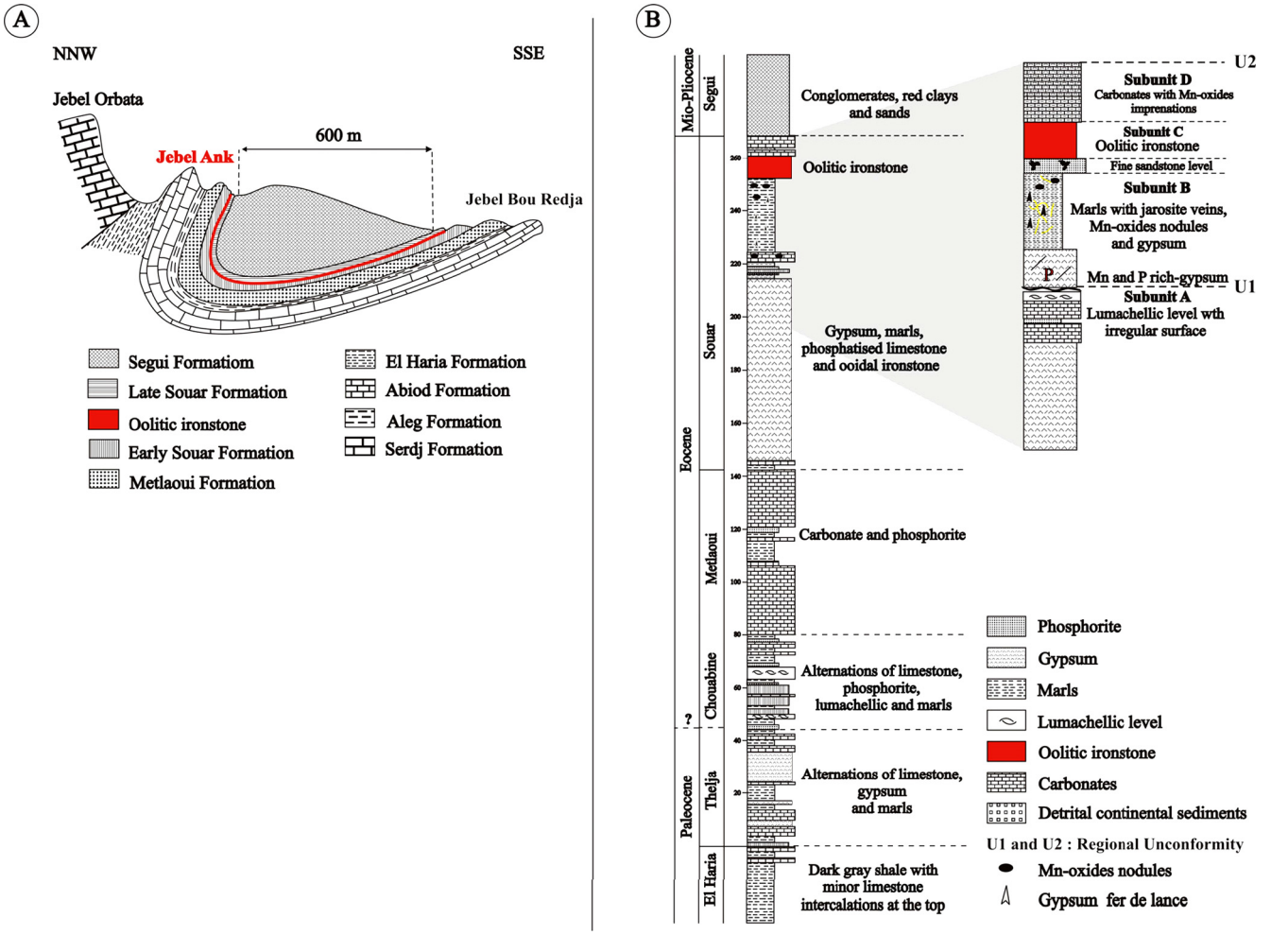

Fig. 2. (A) NNW-SSE cross section located through the Jebel Ank asymmetric-syncline (after M'hamdi, 1984). (B) Stratigraphic column interpreted from the descriptions of Sassi (1974) and M'hamdi (1984).

bottom to mainly smectite at the top) containing thin limestone alternations.

The Late Paleocene-Early Eocene series (Metlaoui Group) is about 140 m-thick and is divided into three formations (Fig. 2B). At the base, the Thelja Formation (Late Paleocene) is a 45 m-thick dominantly evaporite sequence. The base is composed of a lenticular lumachellic bed containing celestite nodules and isolated centimeter sized crystals. Upwards, the sequence shows alternations of dolomitic marls, marly limestones, laminated dolomite and gypsum. The top of the series consists of a lumachellic layer bounded by an erosional discontinuity. The Chouabine Formation (Thanetian-Early Ypresian) is a 40 m-thick phosphorite series. The base is composed of a dolomitic bed overlain by a phospharenite with a brown clayey matrix. The top is composed of an alternation of marls and phosphorite, lumachelle, clayey dolomite and soft phospharenite. Finally, the Metlaoui Formation *sensu stricto* (*s.s.*) (Ypresian-Lutetian) is 60 m-thick and consists of two carbonated layers (bioclastic dolomites) separated by fine feldspars rich-phosphorite layers.

The Souar Formation is subdivided into three lithological units; the lower Souar is about 120 m-thick and is composed of massive gypsum. The middle Souar is represented by alternations of marls containing low amounts of phosphorite and glauconite and is topped by a thin bedded dolomite with manganese oxides. The upper Souar (40 m-thick) that contains the oolitic Fe-mineralization is subdivided into four subunits (Fig. 2B). The lower subunit A corresponds to a carbonate layer above massive gypsum with minor phosphorites. A shell rich layer with an erosional discontinuity occurs at the top of the unit. This unit shows narrow lateral facies variations and the top is marked by an unconformity surface (U1, Fig. 2B).

The subunit B is mainly made of compact manganiferous gypsum (10–15 cm), red clays (smectite and trace of alunite-kaolinite) and gypsum rich-clays with yellow jarosite veins and gypsum crystals (Fig. 3A, B and C). This subunit occurs at the base of a manganiferous gypsum interval, outcropping along both the northern and southern flanks. This subunit is considered to be a marker level (M'hamdi, 1984).

The subunit C shows many facies variations and is the main host to oolitic ironstone mineralization (Fig. 3D). The base starts with a very fine white sandstone level (10–20 cm) mottled by Mn-oxyhydroxides, passing laterally to the west into clays. Absence of an unconformity between the subunits B and C indicates that the transition from clays to sandstone was regressive. Conversely, the top of subunit C is marked by the scarcity of oolites in favor of clays and carbonate sedimentation (subunit D) and can be interpreted as evidence for a transgressive event. Consequently, the oolitic level would correspond to a period of ending regression and then renewed transgression. M'hamdi (1984) indicated that the oolitic level pinches out laterally and progressively into green clays similar to those of the subunit B. The transition zone between the oolitic level and green clays

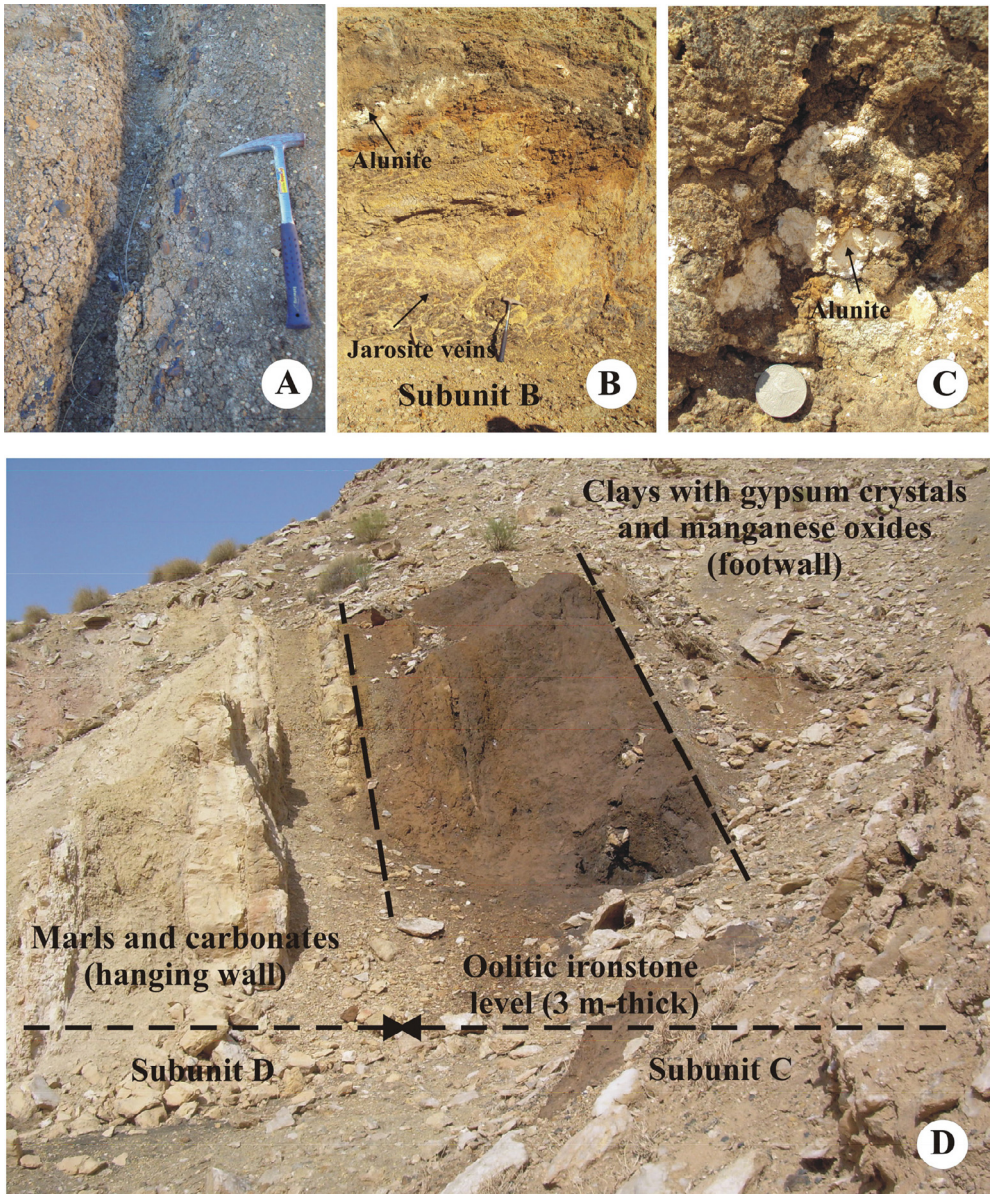

Fig. 3. (A) Manganiferous mud-facies of the subunit B showing centimetric Mn-nodules. (B) Transition between subunit B-subunit C. Subunit C starts with an interval of white clays stained by manganese and Fe-oxides. The subunit C begins with a manganiferous-gypsum interval followed by green clays passing vertically to ocher and mottled clays with manganese nodules. Jarosite concretions and veins occur throughout this clay interval. (C) Fine-grained alunite of the subunit B, having a kaolinite-like appearance. (D) Outcrop view of the oolitic ironstone interval featuring original sedimentary stratification. The oolitic interval was termed by subunit C as defined by M'hamdi (1984). The oolitic interval is about 3 m-thick. The contrast between the brown banding interval and dark ironstone interval produces a distinctive speckled appearance. (For interpretation of the references to colour in this figure legend, the reader is referred to the web version of this article.)

corresponds to green clays with red clay-pockets with ferruginous oolites.

The subunit D (about 3.5 m-thick) is mainly of thin carbonates and is separated from the unit C by clayey dolomite (0.2–0.5 m) (Fig. 3D). The thickness of the mineralized level decreases from the northern flank (5 m-thick) towards the southern flank (0.3–0.1 m-thick) of the synclinal structure. In the northern side, the oolitic mineralized level is almost vertical and passes through the normal with a 20–30° dip on the southern side (Fig. 2A). Mio-Pliocene sediments are discordant on top of the underlying formation and are made of a complex of detrital materials showing a conglomeratic level at the base. The thickness of the Mio-Pliocene sediments is >500 m (Fig. 2A).

The age of the Fe-oolitic mineralization is controversial. It was attributed to Middle Eocene by Berthon (1922), but to the Miocene by Burollet (1956) based on the interpretation that it represents the lateral equivalent of the Beglia Formation. Sassi (1974) placed the Fe-oolitic mineralization in the Souar Formation (Late Lutetian-Priabonian) on the basis of the continuity of the geological record. M'hamdi (1984) maintained the same subdivisions as Sassi (1974) and further subdivided the upper unit of the Souar Formation into four subunits (Fig. 2B). Our study follows that of Sassi (1974) and M'hamdi (1984) in placing the oolitic ironstone level in the Souar Formation.

3. Sampling and analytical methods

Four high-grade ore samples were collected from the Jebel Ank deposit (northern flank of the synclinal structure) and investigated by a variety of mineralogical, petrographical, and geochemical techniques.

The samples were prepared as polished thin sections for petrographic study under transmitted polarizing and reflected light microscopes. The mineralogical analyses of samples were carried out by XRD analysis with a Philips X'Pert diffractometer using CuKa radiation (1.54060 Å). Diffraction data were collected in the range from 3 to 70 and interpreted using X'Pert HighScore Plus software. The accelerating voltage and filament current were maintained at 40 kV and 40 mA, respectively. The bulk mineralogy was determined by semi-quantitative (±5%) XRD. The diffraction analyses were carried out in the Department of Geology, Faculty of Sciences of Tunis, Tunisia.

The major element oxide contents (SiO_2, Al_2O_3, Fe_2O_3, K_2O, Na_2O, MgO, CaO, MnO and TiO_2) of the high-grade samples were determined by atomic absorption spectroscopy. Loss on ignition (LOI) was measured from the total weight after ignition at 1000 °C for 2 h. Trace and rare earth element contents were determined by ICP-MS using an Elan DRCe (Perkin Elmer/SCIEX) instrument at the Department of Earth Sciences, Università della Calabria, following the method described by Garnit et al. (2012).

SEM-EDS analyses were performed on polished sections, using a scanning electron microscope (ESEM FEG, QUANTA200, Philips), equipped with an energy dispersive X-ray analyzer with a Si/Li crystal detector (GENESIS-4000, EDAX). SEM analyses were carried out at the Department of Earth Sciences, Università della Calabria, Italy.

In situ chemical analyses were performed by LA-ICP-MS from individual oolites mounted on polished sections and carried out at the Department of Earth Sciences, Università della Calabria, Italy, using an Elan DRCe (Perkin Elmer/SCIEX), operating either in normal mode as a standard ICPMS instrument or in a dynamic reaction cell (DRC), connected to a New Wave UP213 solid-state Nd-YAG laser probe (213 nm). Calibration was performed using the glass reference material NIST 612–50 ppm (Pearce et al., 1997) in conjunction with internal standardization applying FeO concentrations (Fryer et al., 1995) from scanning electron microscopy with energy dispersive X-ray spectroscopy (SEM-EDX) (Francesco et al., 2005). In order to evaluate possible errors within each analytical sequence, determinations of trace elements were also made on a BCR 2G glass reference material as an unknown sample, and element concentrations were compared with reference values from the literature (Gao et al., 2002). Accuracy, calculated as the difference from reference values, was always better than 10%, and most elements had values in the range of 5%.

Spectroscopic techniques were used to identify and provide complementary information about the composition, crystal morphology, and degree of crystallization and atomic structure of some minerals. FTIR and Raman analyses were carried out at the Department of chemistry and Department of Physics, respectively, at University of Sciences of Tunis. An FTIR spectrum was recorded using a KBr pellet at room temperature by an Agilent ATR spectrometer in the wavenumber range of 4000–400 cm^{-1} using four scans with 2 cm^{-1} spectral resolution.

Raman measurements were performed at room temperature with a T64000 system equipped with a microscope in backscattering configuration and using the 488 nm Ar^+ laser line for excitation and the incident laser power at 5 mW. The Raman shift was determined with an accuracy of 0.25 cm^{-1}. FTIR and Raman data were interpreted using OriginPro8 software.

4. Results

4.1. Petrography

The ironstone layer is friable, dark brown, sandy-siltstone with oolitic texture. The Fe-oolites show variability in morphology and texture, but consistency in composition (Fig. 4A). The Fe-oolites are dark brown under the petrographic microscope in transmitted plane polarized light. The Fe-oolites are generally spheroidal in shape (Fig. 4B), but they vary from perfectly rounded to ellipsoidal (Fig. 4C and D), and some Fe-oolites have irregular forms (Fig. 4A).

Microscopically, three types of Fe-oolites have been recognized: type 1 are >1 mm and are comparable to Fe-oolites described in many oolitic ironstone deposits. This type is abundant (>90%) and characterized by a large well-developed and concentrically laminated cortex and the absence of a clear nucleus (Fig. 4B). Type 2 Fe-oolites have a large nucleus (e.g. quartz, broken fragment) (Fig. 4E and F) and thin laminated cortex (Fig. 5A). Type 3 Fe-oolites have a crude cortex that shows desiccation features (Fig. 5B); some Fe-oolites have cracks radiating from the nucleus (Fig. 5C).

The mineralogy of Fe-oolites consists of microcrystalline goethite. Many Fe-oolites show radial cracks suggesting post-formation modifications due to volume changes (dehydration) and/or compressional forces (Fig. 4B and Fig. 5C). Internally, Fe-oolites are made up of alternate light and dark, thin, nearly continuous concentric layers of goethite. The number of concentric layers varies from less than ten to up to several dozen in a single oolite.

The concentric layers are generally continuous, and the thickness varies within and among oolites. The nuclei of Fe-oolites typically have no consistent shape and can vary from rounded to subangular (Fig. 5C and D). The contact between the nucleus and the cortex, and the cortex and the surrounding matrix between oolites, ranges from sharp to gradational, although sharp transitions are more common (Fig. 5E).

Two types of cracks occur inside Fe-oolites and broken Fe-oolite fragments (Fig. 4C and D), locally present in the same Fe-oolite. Cracks of the first type are contemporary to oolitization, occur within oolites and show concentric and radial orientations. Circular cracks are defined by separation between two successive layers of cortex (Fig. 4B). Radial cracks often extend to the edge of the oolite. In filling of the cracks by cryptocrystalline goethite is often incomplete. The second type of crack formed after oolitization; they are recognized in the broken oolites and are commonly not filled. In other occurrences the cracks are filled with unidentified clays, or Mn-oxyhydroxides (Fig. 5F).

The thickness of the concentric layer varies between 10 and 50 μm. Up to 20 concentric layers were observed in a single Fe-oolite. Quartz occurs as well-sorted detrital grains (up to 0.6 mm) and as microcrystals (less than 0.01 mm) mixed with clay minerals forming agglomerated aggregations. The quartz is not part of the Fe-oolitic layers, but locally occurs at nucleus (Fig. 4E). Quartz grains are generally poorly sorted and angular to subangular (Fig. 5G and H). Apatite occurs as a nucleus in a few Fe-oolites and as fine disseminated grains (1–2 mm) in the matrix (Fig. 5I).

Different stages of evolved glauconites (0.06 mm), or altered glauconite into goethite and phosphatic pellets (0.02 mm), occur as sporadic discrete disseminated grains. Mn-oxyhydroxides in the Fe-oolitic layer occur as diffuse patches filling intergranular space and/or filling late diagenetic cracks in Fe-oolites. Cryptomelane forms centimeter sized nodules in the subunit B (Fig. 3A). Psilomelane fills micro-cracks in some nodules.

Examinations with BSE/EDS show that the concentric structure of the Fe-oolite seems lacking element zonation. It shows that the concentration of Fe in three types of Fe-oolites is independent of the concentrations of Al, Si, P, Ca, K, and Mn (Fig. 6A, B and C). Fig. 6D demonstrates the typical high Fe concentration compared to other elements. No trace of precursor clay minerals has been identified by XRD and no clay particles have been observed by SEM. Silica occurs as discrete areas of high concentration and is not associated to other elements. The areas of high Si concentration correspond to detrital quartz. High Ca concentration is usually associated with areas of higher P concentration (apatite).

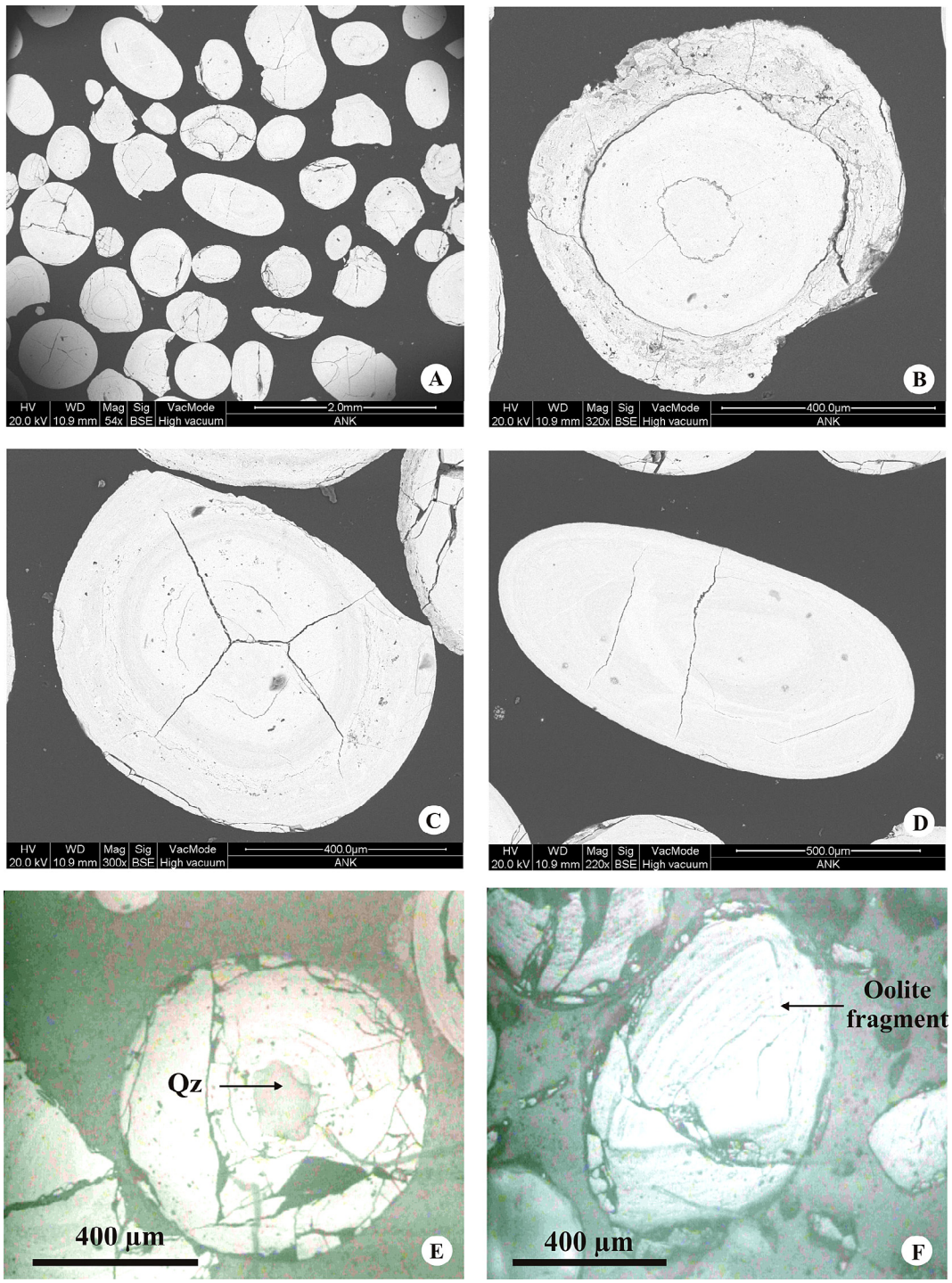

Fig. 4. (A) SEM and reflected light microphotographs of a polished section showing the different morphologies of Fe-oolites. Fe-oolites were handpicked under binocular microscope after washing and granulometric partition. (B) Type 1 Fe-oolite showing very small or not well defined nucleus, the concentric layers contain variable amounts of goethite. The large concentric layer surrounds the earlier core. (C) Type 3 Fe-oolite showing radial and symmetrical cracks. (D) Ellipsoidal shaped oolite showing tangential cracks. (E) Type 2 Fe-oolite showing sub-angular quartz as its nucleus. (F) Type 2 Fe-oolite showing angular fragment scattered in new oolitization.

Jarosite (pale yellow) and alunite (white) are very-fine-grained but are intimately mixed with associated minerals such as clays, quartz, and Mn-oxyhydroxides spread diffusely through other clay minerals.

4.2. Mineralogy

All Fe-oolites are composed of goethite (80–90%). No siderite and/or hematite were detected, in either the oolites or the matrix. Fig. 7A shows the XRD patterns of goethite. Goethite has been identified by the reflection (1 1 0) of d = 4.177 Å which fits the theoretical value (d = 4.18 Å). The slight broadening of the XRD peaks may be due to the poor crystallinity, impurities, Al replacement and small particle sizes. No clays (e.g. chamosite, chlorite) and/or hematite phase were detected by XRD analysis of pure Fe-oolites.

In goethite, (1 1 0) and (1 1 1) reflections have d-spacing values (4.177 and 2.443) lower than the theoretical ones (4.179 and 2.449), respectively (Table 1). This means that goethite is not

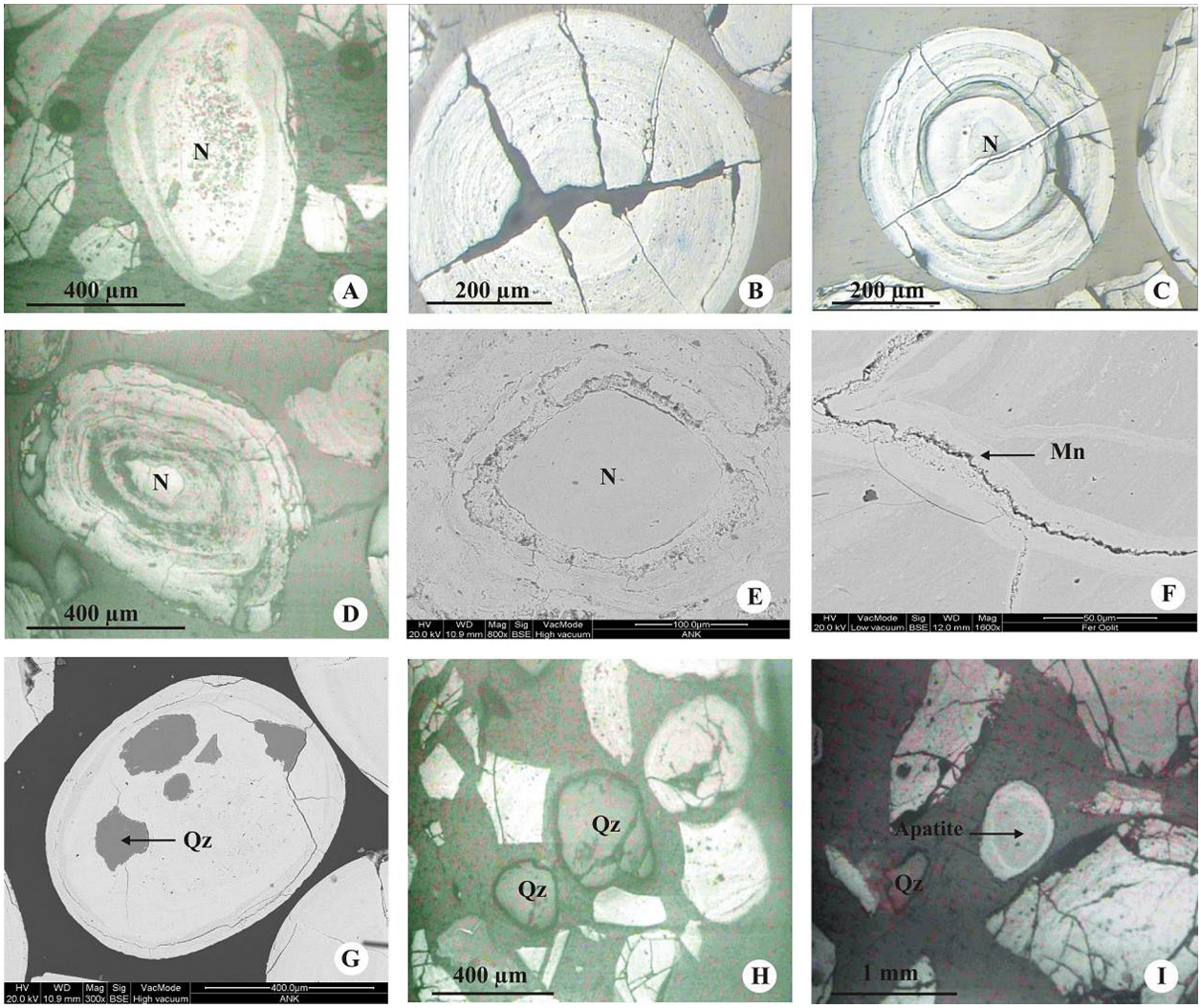

Fig. 5. SEM and reflected light microphotographs of polished sections. (A) Type 2 Fe-oolite with large nucleus and thin laminated cortex. (B) Type 3 Fe-oolite with crude cortex showing radial and tangential micro-cracks with dislocation of fragments. (C) and (D) examples of nucleus shapes that vary from rounded to sub-angular. (E) Sharp contacts between nucleus and the successive concentric layers. (F) Mn-oxides filling micro-cracks inside the Fe-oolite. (G) Sub-angular quartz crystals in the Fe-oolite. (H) Sub-angular quartz in the matrix. (I) Rounded carbonate-fluorapatite grain inside the Fe-oolite.

stoichiometric and contains a number of substitutional cations isovalent or heterovalent to Fe^{3+}. Among all Fe-substituting elements, Al is generally most dominant. Following the method proposed by Schulze (1984), the Al^{3+} content in the goethite structure was calculated based on the position of the peaks corresponding to the d (1 1 0) and d(1 1 1) of goethite (mole % Al = 1730–572c), which were determined from the diffractograms. The results indicate an Al-substitution in goethite of about 5 mol%.

Trace to minor amounts of Mn-minerals occur associated with the Fe-oxyhydroxides in the oolitic ironstone layer. Cryptomelane [K (Mn_7^{4+}, Mn^{3+}) O_{16}] is the main Mn-oxide mineral which was identified by the (3 1 0) reflection (d = 3.116 Å, 2θ = 28.647°) as well as other less intense reflections (Fig. 7B). Open space filling secondary manganese minerals such as psilomelane [$Ba(Mn^{2+})(Mn^{4+})_8O_{16}(OH)_4$] are developed in cracks and between goethite layers.

Evidence for jarosite and small amounts of alunite within marls of the subunit B, below the ironstone layer is provided by XRD analysis (Fig. 7C and D). Jarosite [$NaFe^{3+}{}_3(SO_4)_2(OH)_6$] was identified by XRD based on d = 3.06 Å (2θ = 29.160°). Alunite [$KAl_3(SO_4)_2(OH)_6$] was determined based on (1 1 3) reflection d = 2.985 Å (2θ = 29.928°), but it is also possible that based on their solid solution series chemistry and similar d-spacings, a proportion of an intermediate alunite-natroalunite (d = 2.96 Å, 2θ = 30.168°) end-member may also be present.

Gangue minerals present in the layer include smectite, kaolinite, quartz, gypsum, carbonates, carbonate-fluorapatite, and glauconite. The matrix (10–20%) consists mainly of smectite (70–80%), kaolinite (20–30%) and quartz. Gypsum is locally present, most likely due to recent superficial reworking.

4.3. Spectroscopy

The IR spectra of goethite from the Fe ore was measured over the 400–4000 cm^{-1} spectral range (Fig. 8A). The IR bands of goethite can be used to identify the degree of crystallinity and the extent of Al for Fe-substitution in the goethite structure (e.g. Schulze and Schwertmann, 1984; Cambier, 1986). According to Chukanov (2014), the IR bands assigned to goethite are located at 410, 465, 593, 660, 797, 890, 1000, 1080, 1640, 1770, 3120 and 3350 cm^{-1}. Assignment of IR bands of goethite was made on the basis of previous works (e.g. Cambier, 1986; Salama et al., 2015). The most characteristic IR absorption bands of the studied goethite are present in the low frequency region (<1000 cm^{-1}). Goethite showed major bands at the following positions (cm^{-1}): ν-OH stretching vibration at 3120, δ-OH in *a-b* plane bending vibration

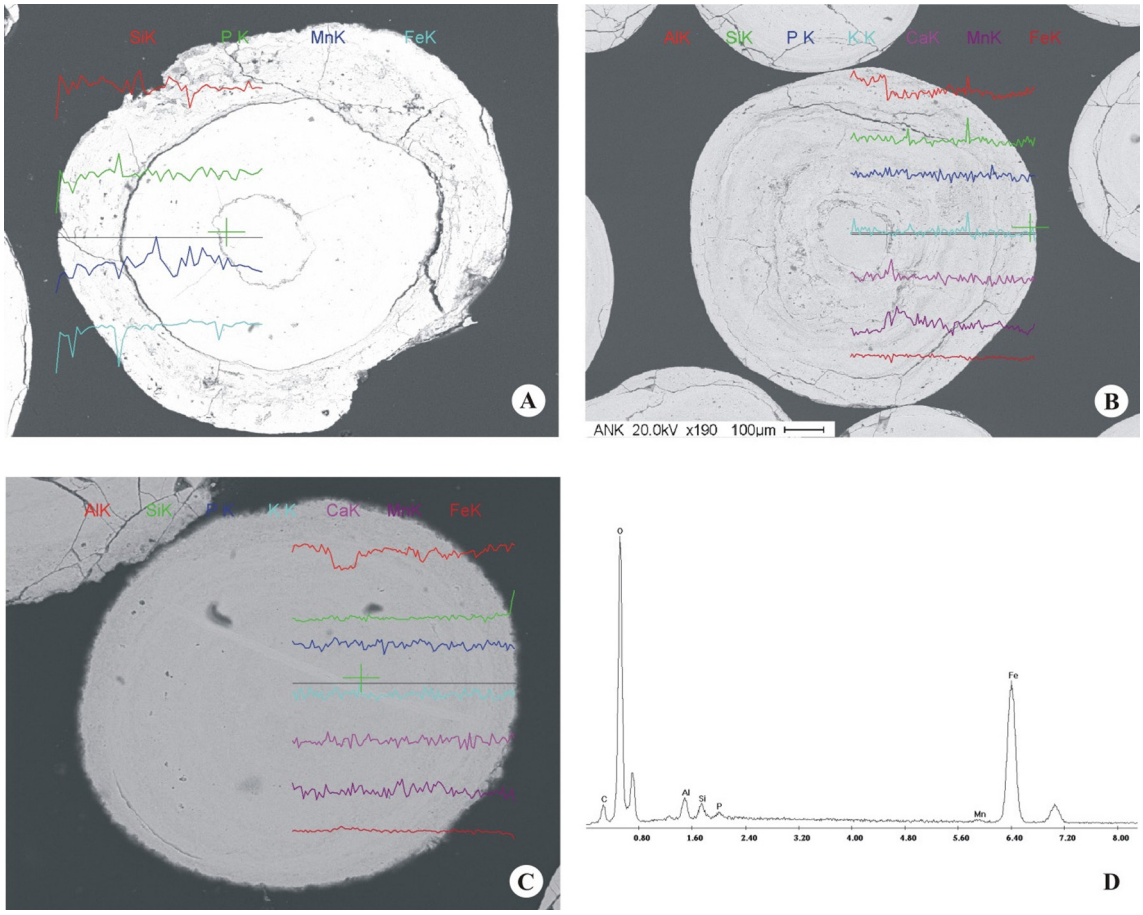

Fig. 6. Back-scattered images of the type 1 Fe-oolite and element profiles showing the distribution of Fe, Si, Al, Mn, P, K and Ca inside of a oolite cortex. (A) and (B) type 1 Fe-oolite. (C) type 3 Fe-oolite. (D) EDS spectra of goethite. Small Si and P peaks are from quartz and carbonate-fluorapatite.

at 890, γ-OH out of plane bends vibrations at 791 and 631. The absorption bands located at 890 and 791 cm^{-1} were ascribed to the Fe–OH in plane and out of plane bending vibrations, respectively. The IR band at 1644 cm^{-1} is close to the position of H_2O bending vibrations.

The complete disappearance of the adsorption band at 3660 cm^{-1} indicates that phosphorous was adsorbed on the surface of the iron oxyhydroxides (Cornell and Schwertmann, 2003). The presence of carbonate-fluorapatite corroborates the possibility that phosphates can be easily adsorbed on the surface of goethite. The separation between the two bands, δ-OH and γ-OH is 99 cm^{-1}, could indicate limited levels of Al for Fe-substitution (Cornell and Schwertmann, 2003). These IR parameters of Jebel Ank goethite match with the goethite formed in shallow marine environments like in the Bahariya Depression (Egypt), reported by Salama et al. (2015).

Jarosite (Fe > Al) and alunite (Al > Fe) IR spectroscopy are sensitive to vibrational modes of OH^-, H_2O, H_3O^+, SO_4^{2-}, and Fe–O bonds (Adler and Kerr, 1965; Kubisz, 1972; Serna et al., 1986; Drouet and Navrotsky, 2003; Bishop and Murad, 2005; Swayze et al., 2008). The fundamental stretching and bending vibrations observed for the studied samples correspond to SO_4^{2-} and OH^-. Fig. 8B and C show the infrared-active fundamental absorptions of jarosite and alunite, which have many detectable vibrational absorptions. Assignment of bands was made on the basis of previous works (Bishop and Murad, 2005; Murphy et al., 2009). The spectra of jarosite and alunite are very similar. In the high wavenumber region, above 3000 cm^{-1}, the infrared spectra of jarosite and alunite show a very strong peak of VOH stretching vibration lying at 3353 cm^{-1} and 3483 cm^{-1}, respectively. Several strong absorptions are present, centered between 1000 and 1250 cm^{-1}. The strongest bands are due to the V3 (SO_4^{2-}) stretching vibration and are observed as a doublet near 1070–1090 and 1170–1220 cm^{-1}. In the intermediate position between the OH stretching position and V3 (SO_4^{2-}) stretching vibration, two prominent IR bands at 2359 cm^{-1} and 2342–2339 cm^{-1} are due to 2V3 (SO_4), 2δ (OH). A doublet of V4 (SO_4^{2-}) vibrations is observed near 669 cm^{-1} and 629 cm^{-1} for jarosite and 665 cm^{-1} and 625 cm^{-1} for alunite. Alunite has an out-of-plane band γ(OH) at 595 cm^{-1}, absent in jarosite. The characteristic IR bands are in agreement with those for standard jarosite-alunite compounds.

For Raman measurements, rough and polished samples were used. Fig. 9 shows the Raman spectrum (200–1000 cm^{-1}) of goethite. The Raman bands assigned to goethite are located at 291, 390, 471, 543, 681 and 990 cm^{-1} (de Faria et al., 1997; Ciobotă et al., 2012). The Raman spectra of goethite display a sharp band at 299 cm^{-1}, a broad band at 396 cm^{-1} and another three weak bands at 240, 477, 551, and 679 cm^{-1}. The feature bands of Jebel Ank goethite are similar to that of Al-substituted goethite reported elsewhere (Liu et al., 2013). According to Liu et al. (2013), the substitution of Al results in a shift of feature bands for goethite to higher wavenumbers and the shift is in accordance with the Al content especially for the band at 299 cm^{-1}.

4.4. Geochemistry

Major element oxides, trace and rare earth elements for four high grade samples from the oolitic ironstone layer are reported in Table 2. Fe_2O_3, SiO_2, and Al_2O_3, represent about 81% of all

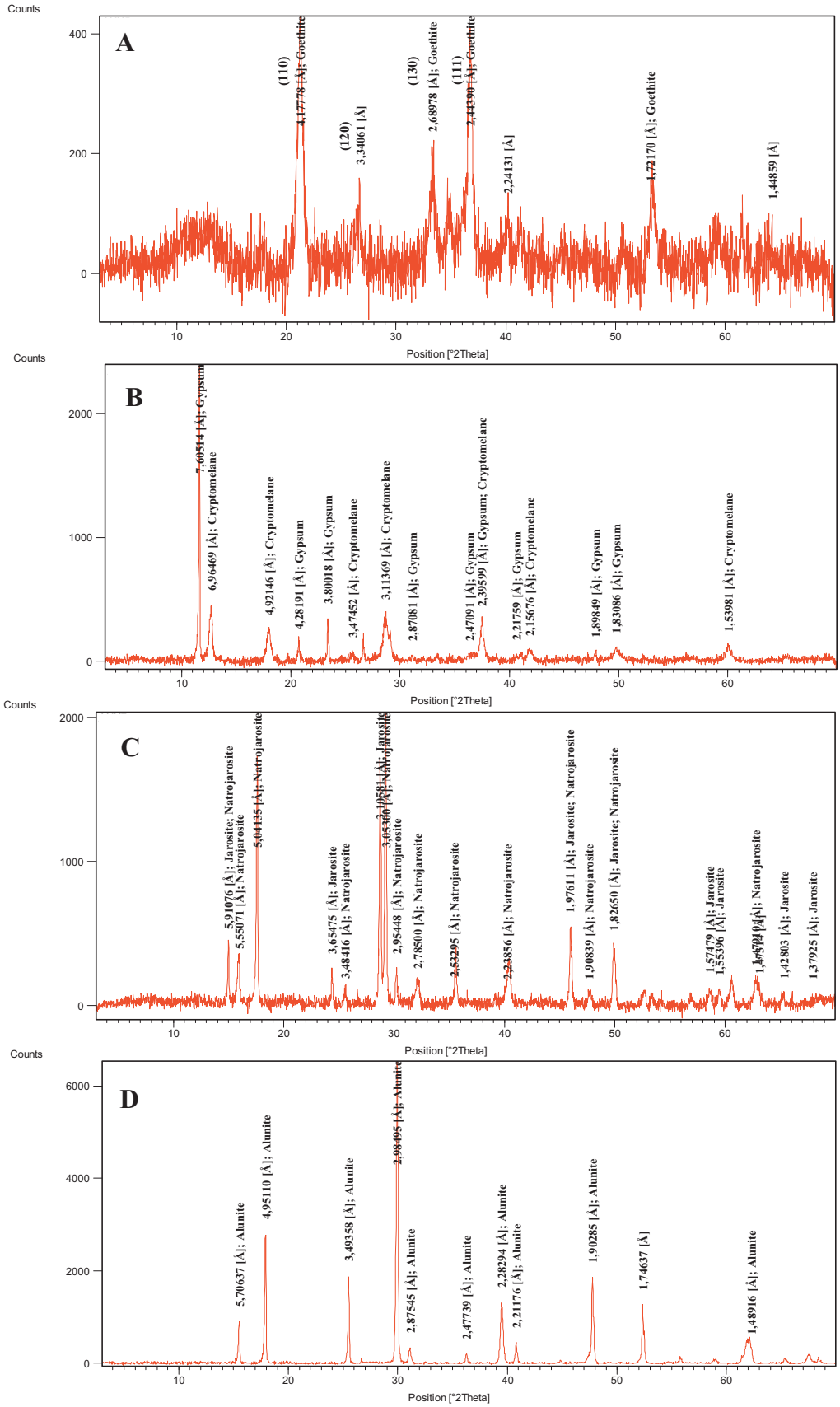

Fig. 7. X-ray diffractograms of (A) goethite, (B) cryptomelane, (C) jarosite, and (D) alunite.

Table 1
Comparison between d-spacing (Å) and reflections of Jebel Ank goethite with reference pattern of pure goethite.

Reflections		(110)	(120)	(130)	(021)	(111)
Reference pattern (01-081-0464)	d-Spacings (Å)	4.179	3.380	2.692	2.584	2.449
Jebel Ank goethite		4.177	3.340	2.689	2.583	2.443

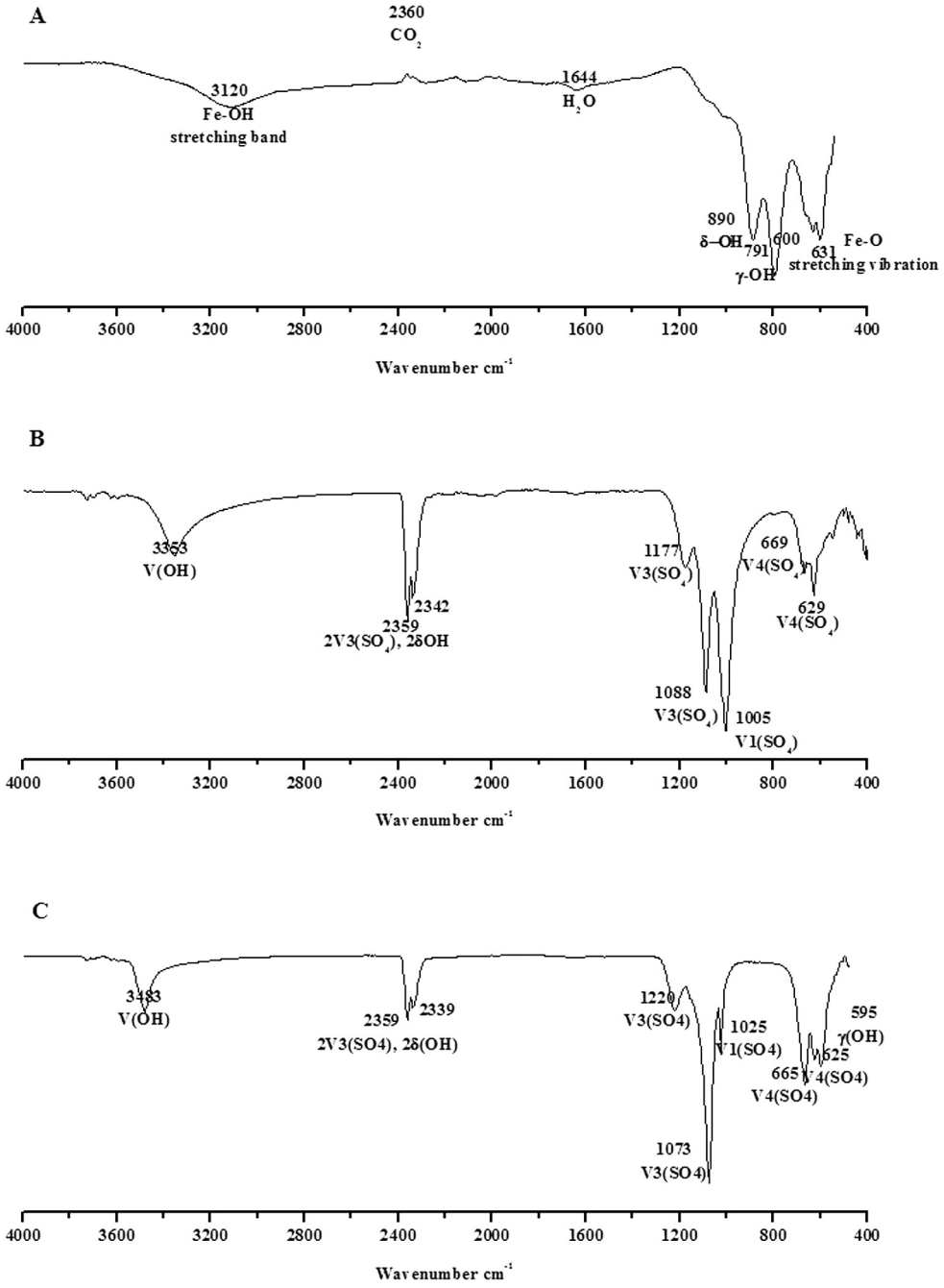

Fig. 8. FTIR spectra, over 400–4000 cm^{-1} spectral range of (A) goethite, (B) jarosite and (C) alunite.

ironstones contents, reflecting the predominance of goethite, clays, and quartz in these rocks. High grade samples from the northern flank average 68% Fe_2O_3. The MnO content is uniformly low, averaging 0.55%. TiO_2, Na_2O and K_2O concentrations are lower than 1%. CaO (average 1.10%) and SO_3 (average 0.35%) are attributed to the presence of gangue minerals, such as carbonates and gypsum. The P_2O_5 (average 1.98%) is linked to the presence of carbonate-fluorapatite. Positive correlations exist between SiO_2 – [Al_2O_3, TiO_2, and Na_2O], while negative correlations occur between Fe_2O_3 – [SiO_2, Al_2O_3, TiO_2, and Na_2O].

All samples show deceasing mean abundance (ppm) of V (8120), Zn (425), Ni (241), Co (123), Cr (114), Sr (106), Y (85), Ba (66), Zr (65), Mo (31), As (30), Pb (28), Cu (16), and Sc (13). The abundance of V reflects its substitution for Fe in goethite

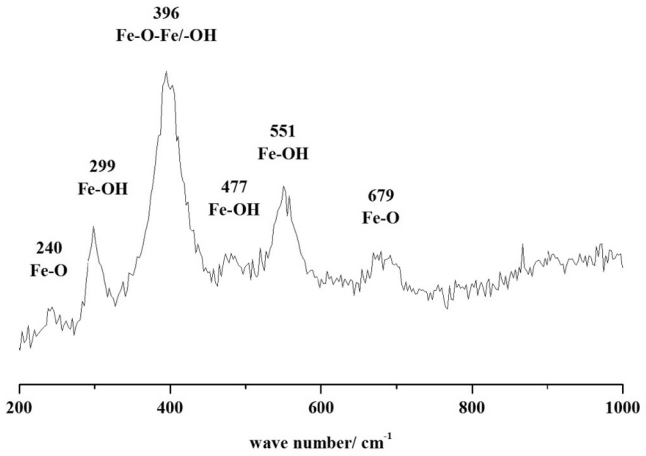

Fig. 9. Raman spectra in the range from 200 to 1000 cm^{-1} of goethite.

(e.g. Schwertmann and Pfab, 1997; Kaur et al., 2009). PAAS-normalized trace elements of bulk samples are enriched in V, Co, Ni, Zn, As, Mo, and Y and are depleted in Cu, Rb, Zr, Nb, Ba, and Hf (Fig. 11A). Positive correlations exist between Fe_2O_3, V, Cr, Co, Ni, Zn, As, Mo, and Y (Table 3).

The cerium anomaly ($Ce/Ce* = 3Ce_N/(2La_N + Nd_N)$), Eu anomaly ($Eu/Eu* = Eu_N/(Sm_N \times Gd_N)^{1/2}$), and Y anomaly ($Y/Y* = 2Y_N/(Dy_N + Ho_N)$) were calculated according to Shields and Stille (2001), where $_N$ refers to normalization of concentrations against the PAAS shale standard (McLennan, 1989). Bulk samples have ∑REE-Y concentrations of 458.9–552 ppm with coherent REE-Y patterns characterized by relative enrichments of HREE and nearly flat MREE (La_N/Yb_N = 0.17–0.24), significantly positive Ce (1.96–2.13), negative Y (0.74–0.84), and moderately positive Eu (1.11–1.16) anomalies (Table 2). La/Ce and Y/Ho ratios vary from 0.13 to 0.14, and 17.8 to 21.3, respectively. Fig. 11B shows the PAAS-normalized REE-Y patterns of bulk samples compared to hydrothermal, hydrogenetic and diagenetic Fe-Mn nodules (after Bau et al., 2014).

Table 2
Major oxides (%), trace and rare earth elements (ppm) and elemental ratios of four bulk high grade ore samples from the northern flank.

	ANK9	ANK10	ANK11	ANK12
SiO_2 (%)	7.81	7.77	7.67	8.20
TiO_2	0.14	0.14	0.12	0.16
Al_2O_3	4.62	4.60	5.07	6.12
Fe_2O_3	68.91	69.48	69.44	66.88
MnO	0.48	0.49	0.68	0.55
MgO	0.78	0.79	0.8	0.79
CaO	1.2	1.21	1.11	0.89
Na_2O	0.10	0.10	0.10	0.12
K_2O	0.18	0.18	0.16	0.11
P_2O_5	2.01	2.03	1.89	2.02
SO_3	0.40	0.38	0.25	0.37
LOI	12.78	12.89	12.76	13.56
Total	99.41	100.06	100.05	99.77
Sc (ppm)	11.10	12.33	14.67	15.09
V	802.7	912.6	948.9	584.2
Ba	74.03	66.83	58.89	64.11
Sr	110.6	123.5	93.04	98.29
Y	83.22	91.60	92.40	73.12
Zr	56.04	62.73	67.15	76.45
Cr	114.4	118	116.5	110.2
Co	112.2	137.8	149.3	92.82
Ni	239.6	245.2	253.4	228.7
Cu	10.67	15.02	17.11	22.67
Zn	445.9	466.0	453.6	337.3
As	35.46	37.01	38.78	10.62
Pb	18.67	24.09	33.56	36.23
La	26.00	32.8	37.11	27.33
Ce	206.00	211.8	226.4	192.9
Pr	14.20	16.39	17.34	13.82
Nd	79.00	78.14	81.73	67.36
Sm	18.66	18.58	18.43	15.66
Eu	4.57	4.52	4.68	4.02
Gd	18.43	19.80	19.65	17.27
Tb	3.24	3.35	3.21	2.81
Dy	17.76	18.92	18.88	16.21
Ho	4.22	4.29	4.45	4.10
Er	11.71	12.58	12.96	10.75
Tm	1.66	1.71	1.79	1.61
Yb	11.12	11.59	11.26	10.34
Lu	1.75	1.84	1.84	1.59
∑REE-Y	501.54	527.91	552.13	458.89
La/Ce	0.13	0.15	0.16	0.14
La_N/Yb_N	0.17	0.21	0.24	0.20
Y/Ho	19.72	21.35	20.76	17.83
Y_N/Ho_N	0.75	0.81	0.79	0.68
Ce/Ce^*	2.10	1.98	1.96	2.13
Eu/Eu^*	1.16	1.11	1.16	1.15
Y/Y^*	0.79	0.84	0.83	0.74

Table 3
Inter-element correlations showing the major trends (Pearson correlation coefficients at P < 0.05, number of samples is 4).

	Al	Si	V	Cr	Mn	Fe	Co	Cu	Ni	Zn
Al	1									
Si	0.62	1								
V	0.97	0.80	1							
Cr	0.93	0.85	0.98	1						
Mn	0.74	0.92	0.87	0.85	1					
Fe	0.66	0.99	0.83	0.85	0.96	1				
Co	0.32	0.94	0.54	0.63	0.77	0.91	1			
Cu	0.13	0.86	0.38	0.47	0.68	0.82	0.98	1		
Ni	0.92	0.87	0.98	1.00	0.88	0.88	0.67	0.51	1	
Zn	0.91	0.87	0.98	0.96	0.95	0.90	0.65	0.50	0.97	1

More than 0.95 is significant at 0.05 level, and number of samples is 4.

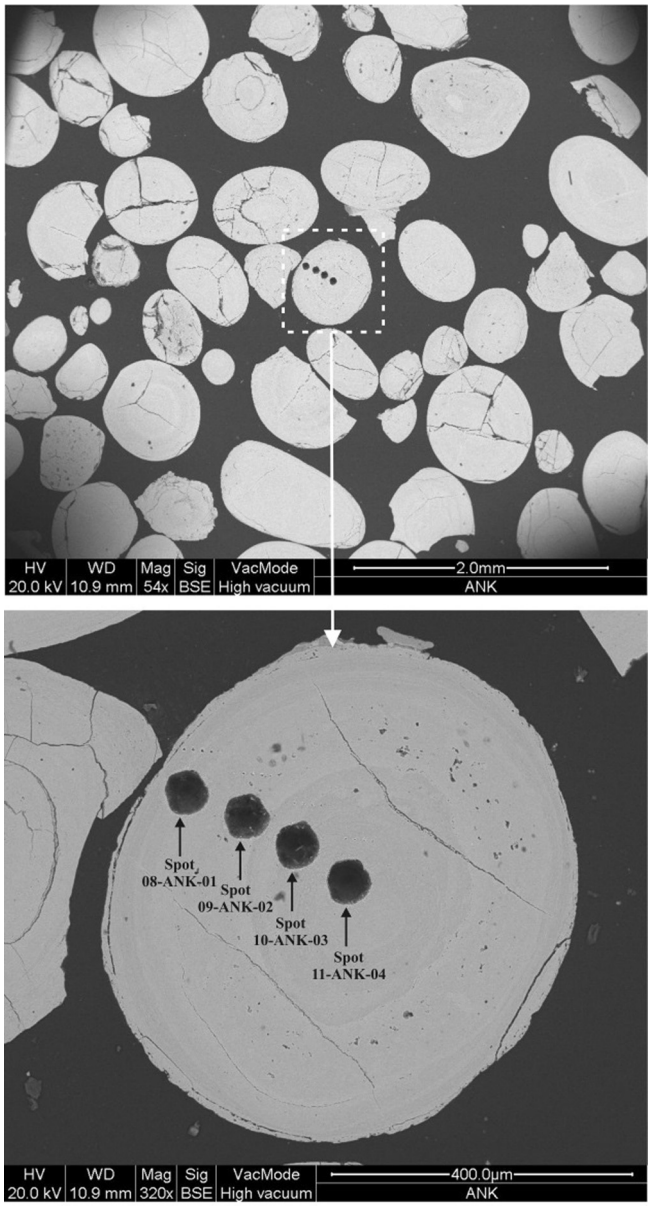

Fig. 10. BSE microphotographs showing LA-ICP-MS analysis inside type 1 Fe-oolite.

In addition to the bulk chemical analyses, detailed profiles within Fe-oolites were measured by SEM-BSE (Fig. 6) and LA-ICP-MS (Fig. 10). Using SEM-BSE, chemical mapping was conducted to examine the distribution of the major elements within different Fe-oolite types. The main components include Al, Si, P and minor Ca, Mn, and K. The element maps for Ca and K show that they are homogeneous in their distribution with concentrations limited to <1%. Fe, Al, Mn and Si concentrations are variable, and depend on the Fe-oolite type. Fe-oolites type 2 and 3 display much greater element variations. In addition to the nearly uniform phosphorus distribution in the oolite, the core of this Fe-oolite is rich in P. Phosphorous (0.66–1.45%) may be concentrated in micro-areas, which is predominantly related to the presence of carbonate-fluorapatite.

Concentrations of trace elements in the Fe-oolite type 1 are shown in Table 4. Elements such as V, Ni and Zn occur in high concentrations (>500 ppm), while Co, As, Cr and Sr are present in lower concentrations (80–300 ppm). The average contents obtained for Y, Ba, Zr and Nb are 85.2, 66.2, 55.8 and 3.64 ppm respectively. Cu concentrations average 6.9 ppm. In comparison with the trace element concentrations of the PAAS given by Taylor and McLennan (1985), the Fe-oolites are relatively enriched in V, Co, Ni, Zn, As, Mo and U; and relatively depleted in Ba, Zr, Cu, Rb, Nb, Sn, Sb, Hf and Ta; while Sc, Sr, Cr, Pb and Th are very similar (Fig. 11A).

The ∑REE-Y concentrations of type 1 Fe-oolite range between 341.2 and 736.9 ppm (Table 4). La/Ce ratios range from 0.10 to 0.17 (Table 4). PAAS-normalized REE-Y patterns exhibit a significantly positive Ce anomaly ($Ce/Ce* > 1.0$, Table 4) but negligible light to heavy-REE fractionation ($La_N/Yb_N = 0.11–0.33$, Table 4), weak positive Eu-anomaly ($Eu/Eu* = 1.13–1.22$, Table 4) and negative Y anomaly (average $Y/Y* = 0.79$). The goethite display a negative Y-anomaly ($Y_N/Ho_N = 0.82–0.88$) and have Y/Ho molar ratios between 21 and 23, very close to that of PAAS (Y/Ho = 26, Taylor and McLennan, 1985).

Bulk-sediment elemental data are consistent with type 1 Fe-oolite microanalyses, although complementary trace and rare earth elements data for other Fe-oolite types arerequired for confirmation. This demonstrates that the trace element and REE-Y bulk chemistry of the oolitic ironstone are dominated by the composition of the Fe-oolites, and is unaffected by the enclosing siliciclastic matrix. A Pearson correlation demonstrates a close association within specific element groups, ascribed to largely mineralogical controls, such as goethite (Fe_2O_3; V, Cr, Ni, Zn, and REE-Y) and silicates (quartz, clays; SiO_2, TiO_2, Al_2O_3, MgO, K_2O, Ba, Hf, Nb, Rb, and Zr).

5. Discussion

5.1. Depositional environment and origin of Fe-oolites

The depositional environment and origin of oolites has long been a subject of speculation and discussion. Several depositional environments have been proposed for oolitic ironstone: shallow marine (e.g. Macquaker et al., 1996; Donaldson et al., 1999; Sturesson, 2003), offshore transition marine (Burkhalter, 1995);

Table 4
Chemical composition of Jebel Ank goethite (four spot analyses of type 1 Fe-oolite).

Element	08-ANK-01	09-ANK-02	10-ANK-03	11-ANK-04
Na	429.2	384.2	446.7	464.0
Mg	9028	6607	7897	7881
Al	50,955	30,489	40,651	41,756
Si	17,202	15,940	15,659	15,426
P	6675	7390	10,841	14,547
K	424.7	383.6	501.2	540.8
Ca	2885	3351	3183	2806
Sc	21	8.81	12.87	13.04
Ti	773.5	397.6	535.6	583.3
V	1957	1367	1578	1567
Cr	301.7	82.0	125.2	149.5
Mn	7202	5548	6048	5210
Co	217.3	197.6	173.5	168.2
Cu	8.46	7.84	5.98	5.43
Ni	687.5	518.4	549.9	560.4
Zn	755.2	596.5	650.7	622.4
As	196.5	209.6	221.1	206.5
Rb	7.15	5.16	6.40	6.50
Sr	118.2	107.9	121.4	115.6
Y	84.06	105.9	76.29	74.7
Zr	76.69	35.97	53.05	57.62
Nb	5.49	1.92	3.34	3.82
Mo	46.39	39.46	47.36	46.11
Sn	2.21	0.44	0.88	1.05
Sb	0.39	0.28	0.31	0.10
Ba	61.57	73.03	69.33	61.05
La	17.43	58.6	18.08	16.38
Ce	162.1	338.6	129.8	111.1
Pr	7.45	21.67	7.11	6.52
Nd	37.47	92.74	32.46	29.82
Sm	12.65	23.34	10.27	10.85
Eu	3.37	5.86	3.10	2.89
Gd	15.51	24.77	13.96	12.82
Tb	2.77	3.95	2.58	2.46
Dy	19.9	24.99	18.5	19.17
Ho	3.88	4.83	3.62	3.21
Er	11.91	14.7	10.37	11.61
Tm	1.98	2.01	1.85	1.76
Yb	11.58	13.25	11.79	11.38
Lu	1.61	1.74	1.43	1.26
Hf	1.57	0.74	0.90	1.05
Ta	0.20	0.06	0.21	0.09
Pb	53.9	54.51	46.83	47.49
Th	15.34	5.74	9.50	9.62
U	76.5	56.73	66.43	67.8
∑REE-Y	393.67	736.95	341.21	315.93
La/Ce	0.11	0.17	0.14	0.15
La_N/Yb_N	0.11	0.33	0.11	0.11
Y/Ho	21.66	21.93	21.07	23.27
Y_N/Ho_N	0.83	0.84	0.80	0.89
Ce/Ce^*	3.03	2.20	2.57	2.41
Eu/Eu^*	1.13	1.15	1.22	1.15
Y/Y^*	0.79	0.80	0.77	0.78

restricted lagoonal marine (Bayer, 1989); or coastal and deltaic setting environments (Collin et al., 2005). They are usually encountered in simply folded shallow shelf areas, and most typically are close to the transition from non-marine to marine environments and always hosted by clastic sediments at the top of coarsening and shoaling-upward cycles (Maynard and Van Houten, 1992).

Paleogeographically, since the Late Cretaceous and the beginning of the Eocene time the Jebel Ank area was situated on the border of an epicontinental stable platform. Semi restricted lagoons were developed in a low-lying area between two gentle topographic highs: Kasserine Island in the centre and Jeffara Island to the south (Sassi, 1974; Burollet and Oudin, 1980; Winnock, 1980; Chaabani, 1995; Zaïer et al., 1998). This configuration contributed to trapping of Fe-rich sediments in the Jebel Ank area.

Restricted exchanges with the Tethyan Ocean occurred during Ypresian-Lutetian time, as shown by the occurrence of phosphorites. Subsequently, a lagoonal setting allowed the development of massive evaporitic sedimentation and, restricted exchanges with the Tethyan Ocean resumed. The occurrence of a threshold and littoral zone with agitated and oxygenated waters allowed the increase of Eh or pH, therefore causing the precipitation of Fe-oxyhydroxides (e.g. Hem and Cropper, 1959). The oolitic ironstone accumulated in Fe-enriched, but clastic depleted waters, during a transitional stage that developed at the end of a regional regression or at the beginning of transgression. An association with evaporates, minimal siliciclastic input with clay mineral assemblages dominated by smectite, indicates that ironstone deposition accompanied stable warm arid climate conditions that developed during the latest Paleocene-Eocene time.

The studied oolitic ironstone facies suggests that depositional conditions were mainly shallow marine, limited silicates-mixed, relatively agitated, and oxic water. The presence of iron has been observed mainly as true oolites and minor Fe-coatings of oolite fragments and/or detrital quartz grains. Goethite could not be

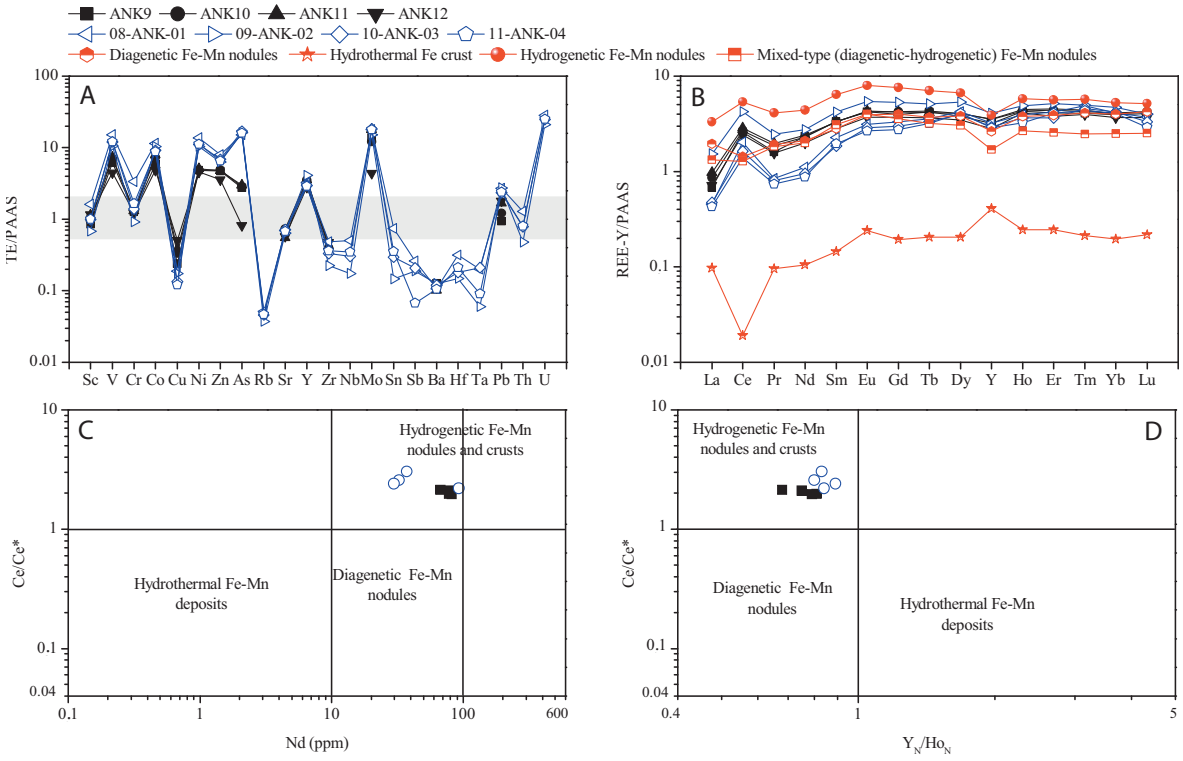

Fig. 11. (A) PAAS-normalized trace elements of bulk samples and Fe-oolite, element ratios greater than 2 are enriched and those below 0.5 are depleted compared to PAAS. (B) PAAS-normalized REE-Y patterns of bulk samples and Fe-oolite showing significant positive Ce anomalies and negative Y anomalies, characteristic of hydrogenetic precipitation. REE-Y patterns of Jebel Ank samples are compared to diagenetic, hydrothermal, hydrogenous and mixed type Fe-Mn precipitates (after Bau et al., 2014). (C) and (D) Plots of the Jebel Ank iron ore in the discrimination diagrams of (Ce/Ce∗ *vs* Nd concentration) and (Ce/Ce∗ *vs* Y_N/Ho_N) (discrimination plots after Bau et al., 2014).

observed replacing/impregnating the matrix or cement. Therefore, iron must have been synchronously precipitated during or just after the sedimentation.

Generally, the fine sandstone footwall level displays very little or no Fe-component. This may be related to a siliciclastic influx into the basin changing the Eh-pH conditions and disturbing the conditions of the Fe-oxidizing. However, there also has been no iron observed in the carbonates of the hanging wall. This may be interpreted as a change in the water chemistry (CO_2 content, Eh-pH, temperature) without siliciclastic influx and can be related to the cooperation of paleoenvironmental, paleoceanographic and paleoclimatic changes.

In contrast to Jebel Ank, it is widely reported that Fe-oolites depositions are often associated with sedimentary and/or structural features (e.g. ripple marks, erosions, cross bedding, and abundance of coarse terrigenous material) indicative of hydrodynamically active setting of their formation (e.g. Mutrux et al., 2008). The studied oolitic level, displays an absence of sedimentary structures, and suggests stratigraphic and sedimentary continuity within the bounding levels.

Geologically, the Fe ore of Jebel Ank, including the underlying Mn-rich ores, occur as simply folded stratiform ores. Evidence supporting an epicontinental environment of deposition for the interval hosting the Fe-mineralization includes the absence of fossils, bioturbations, and fine dominant sediments. The primary nature of the deposit is evident from the primary bedding concordant with those of the bounding levels.

The basal sandstone (80% quartz, feldspars, glauconite, and apatite) of the subunit C marks a detrital period prior to Fe-oolites deposition. Thicker correlative clays deposited in the west suggests a transition from a coastal to deep marine environment. The mineralogical and geochemical consistency of the oolitic layer attests to a uniform environment of formation. However the co-occurrence of chemically deposited minerals (goethite, apatite, carbonates, gypsum/anhydrite and glauconite) and low amounts of detrital minerals (quartz and clays) suggest that formation was in a shallow lagoon environment. The textural features described in this study for the Jebel Ank oolitic ironstone strongly indicate that oolite formation was authigenic; formed essentially in place in relatively shallow, agitated water, and not formed during diagenesis.

Origins of oolites can be linked to: in situ growth or direct precipitation from seawater as true oolites (Hemingway, 1974); crystallization from Fe-oxyhydroxide gel precursors (Harder, 1989), replacement of preexisting aragonite oolites by Fe-rich solutions (Sorby, 1856; Cayeux, 1909; Kimberley, 1979); mechanical accretion of clays with subsequent transformation to Fe-rich phases (Bhattacharya and Kakimoto, 1982; Van Houten and Purucker, 1984; Tobia et al., 2014), ferruginization of calcareous microfossils (Champetier et al., 1987), diagenetic hematitization of precursor green glauconitic clays (Mesaed, 2004; Mesaed and Harbi, 2013), lateritic weathering (Siehl and Thein, 1989), or diagenetic and microbial activity (Dahanayake and Krumbein, 1986; Ciobotă et al., 2012; Salama et al., 2013).

Regarding the origin(s) of Fe-oolites in Jebel Ank deposit, two scenarios have been proposed: Fe-oolite formed originally as chlorite in hydromorphic environment (Solignac, 1930). M'hamdi (1984) suggested mechanical accretion of clays and/or Fe-oxyhydroxide gels in lagoon environment with subsequent transformation to Fe-rich phases.

The petrographic features of the Jebel Ank Fe-oolites, including their symmetrical shape, no sorting, presence of broken oolites, and delicate textural lamina of the oolite cortex, rule out their origin as deposition of sediment transported from a more distant source area. The co-existence of true and broken Fe-oolites that acted as nuclei for larger compound oolites suggests that such

oolites were formed in a relatively agitated environment. However, oolites fragments scattered in these new oolitization events are angular, with no trace of reworking; this implies that oolites haven't experienced significant transport. Fragmentation of the oolites was possibly an in situ process due to dehydration (Adeleye, 1975). The most probable mode of Fe-oolite formation was within a shallow marine environment near, or at, the site of ironstone deposition. In addition, the presence of quartz and apatite (in the nuclei and incorporated into the cortex of the oolites) are reliable indicators of a possible accretionary model for the formation of oolites prior to ferruginization. The absence of carbonaceous oolites in equivalent layers in the surrounding area indicates that the ferruginous oolites are probably primary depositional particles (Salama et al., 2014).

No trace of precursor clay minerals has been identified by XRD and no clay particles have been observed by SEM. However, major oxides, spectroscopic and microchemical analyses show low concentrations of Al (<5 mol%), which rules out any replacement of a precursor clay mineral by goethite (Maynard, 1986; Gehring, 1989; Cotter, 1992; Salama et al., 2014). Microanalyses of goethite, show little aluminum, so derivation by oxidation of Fe-rich silicates is unlikely, and the iron must have been precipitated directly as $Fe(OH)_3$ and progressively oxidized to FeOOH.

This argument suggests that the goethite is of primary origin. Low Al-substitution (10−15 mol%) in goethite prevails in hydromorphic, moderately acidic soils and calcareous environments, while substitution of 15−32 mol% is usually found in goethite from highly weathered soils of subtropical and tropical areas (Fitzpatrick and Schwertmann, 1982; Stucki et al., 1988). The uniform fabrics exhibited by goethite indicate that few mechanisms were involved in its formation. Goethite can form either by inorganic or organic precipitation (e.g. Burkhalter, 1995; Salama et al., 2013). Microbial contribution to the origin of the Jebel Ank Fe-oolite can be suggested.

REE-Y patterns of Fe-oolites show distinctive positive Ce anomalies, indicative of strongly-oxidizing near surface conditions. Similarly a positive Ce anomaly has been found in some weathering profiles on various types of source rocks (Braun et al., 1990). Hydrogenous deposits are represented by a positive Ce anomaly, but hydrothermal deposits are characterized by negative Ce anomalies (Bau et al., 1996, 2014). The studied samples display slight positive Ce anomalies which resemble the pattern of hydrogenous Fe-Mn deposits.

Although the development of low-temperature supergene weathering products underlying the oolitic layer produces a distinctive paragenetic sequence, the occurrence of cryptomelane, jarosite, and alunite in the ironstone sequence can be considered as further evidence of the type of weathering processes that occurred at Jebel Ank. Alunite and jarosite minerals were reported in the Late Eocene tidal clays associated with laminated primary gypsum and Fe-oxide at El Gnater site, central Tunisia (Gaied et al., 2015). Late diagenetic origin in reduced conditions and in evaporitic environment is proposed for alunite. However, jarosite was produced by oxidation of pyrite, which was very abundant in the claystone host rock (Gaied et al., 2015). Their association with the ironstones is considered as a proxy for subaerial weathering and post-diagenetic meteoric water alteration.

The association of few manganese minerals, with abundant goethite, indicates that these minerals were formed from Fe-rich solutions with minor Mn. Fe and Mn were indeed derived from the same source and are fractionated to produce high Fe/Mn ratios. The low Mn/Fe ratio reflects high separation between the two elements in the hydromorphic environment. They are mobile in reducing conditions (Pedersen and Price, 1982), but Mn requires a higher oxidation potential to precipitate than Fe^{2+} (Canavan et al., 2007). It is reported by Baioumy et al. (2013), that the occurrence of Mn ores at the base of the oolitic layer indicates a supergene origin from descending solutions as a source of Mn and Fe due to the higher solubility of Mn compared to Fe. The Fe would have precipitated first in the upper part of the section close to the source of elements, and then Mn would be precipitated in the lower parts, far from the source (Baioumy et al., 2013). The formation of cryptomelane may have occurred at relatively final stages of weathering when local increases in pH and oxidizing conditions prevailed with the presence of the K^+ from smectite-bearing level.

5.2. Possible source(s) of iron and formation of oolitic ironstone

In general, there are different hypotheses regarding the source of the iron in oolitic ironstones. The Fe-enrichment can occur from supergene sedimentary processes (Van Houten and Arthur, 1989; Young, 1989a,b; Burkhalter, 1995; Macquaker et al., 1996) or the Fe-enrichment is hypogene including hydrothermal and/or volcanic sources. Fe-Mn oxyhydroxide precipitates, may be of hydrothermal, hydrogenous, diagenetic or mixed-type (diagenetic-hydrogenetic) origins, this terminology is based on the type of aqueous fluid from which the Fe-Mn oxyhydroxides precipitate (Bau et al., 2014).

Regarding the source(s) of iron for Jebel Ank oolitic ironstone, M'hamdi (1984) suggested two origins: (i) iron has been leached from underlying sediments; (ii) iron was sourced from continental weathering and was transported to the basin of sedimentation. The latter is most likely based on palaoegeographic evidence and the strong correlation between iron, phosphorus and zinc.

The oolitic ironstones clearly have elevated Fe_2O_3, SiO_2, and Al_2O_3 but lesser MnO, and also lower amounts of CaO and MgO. In general, these element concentration trends are similar to those of the Eocene oolitic ironstones in other parts of the world (e.g., El Bahariya Depression, Egypt, as reported in Salama et al., 2012). The negative correlation of Fe_2O_3 with both SiO_2 and Al_2O_3 reflects the decreased deposition of detrital quartz grains and fine-grained detrital clay minerals during Fe-deposition, which attest that goethite is primarily chemically precipitated. Si and Al data from bulk samples and Fe-oolite suggest a hydrogenous origin based on their plotting in the hydrogenous field of the Si−Al discrimination diagram of Choi and Hariya (1992) (Fig. 12A).

The relatively high content of P_2O_5, up to 2%, and low TiO_2/Al_2O_3 (0.2–0.3) may indicate a continental source for the phosphorous and the iron, given that phosphorous generally is believed to be leached from a continental source and then migrates to the sedimentary basin of deposition (Millot, 1964; Chauvel, 1968, 1974; Price, 1976).

High P_2O_5 content are recorded in several oolitic ironstone deposits that ranges from 0.2 to 0.8% but may sometimes exceed 1.5% (Kennedy, 1990). In the oolitic iron ores of Aswan (Egypt), P_2O_5 ranges from 0.3 to 3.4 wt% and is positively correlated with CaO due the occurrence of P mainly as hydroxyapatite as massive grains inside the oolites and/or in the ferruginous groundmass (Baioumy et al., 2017). The apatite in the Jebel Ank iron ores occurs as rounded to subrounded, spherical and massive grains of about 200 μm. Mineralogy shows that this apatite is carbonate-fluorapatite. These evidences suggest the detrital origin of this grains resulting from reworking of preexisting apatite grains.

Oolitic ironstones are recognized as being enriched in many trace elements such as V, Ba, Sr, Co, Zr, Y, Ni, Zn, and Cu (e.g. Olsen et al., 1999; Salama et al., 2012; Tobia et al., 2014). In addition, anomalous P, V, Cr, Ni, Zn, As, Mo, and U are commonly correlated with Fe-oxyhydroxides (Salama et al., 2012).

In the Jebel Ank ironstones some trace elements are enriched relative to PAAS, whereas others are depleted (Fig. 11A). Vanadium is one of the highly enriched elements in the Jebel Ank deposit, generally following Co, Ni and Zn. V content range from 584 to

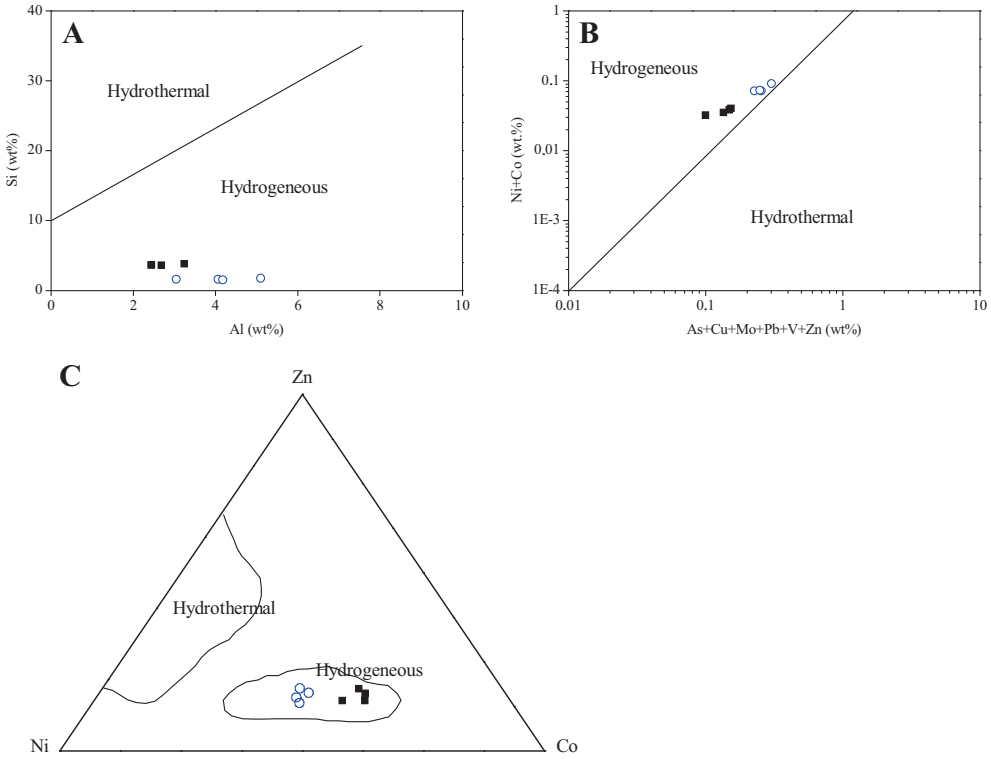

Fig. 12. (A) Si-Al discrimination diagram of Choi and Hariya (1992). (B) Ni + Co vs. As + Cu + Mo + Pb + V + Zn discrimination diagram (Nicholson, 1992). (C) Zn–Ni–Co discrimination diagram (Choi and Hariya, 1992). The studied iron ores plot in the field of hydrogenous origin in all diagrams.

949 ppm (average 812 ppm), higher than Egyptian Bahariya iron ores (31–122 ppm, Baioumy et al., 2014) and similar to pisolitic ores of Ga'ara of Western Desert of Iraq (average 724 ppm, Tobia et al., 2014).

The source of the ferromagnesian elements (Cr, Ni, Co, Sc, and V) is likely to be from basic rocks (Wronkiewicz and Condie, 1987); these elements can be supplied either from the weathering of the basic rocks present outside the basin or by within-basin volcanism (Khan and Naqvi, 1996). Given that there are no indications of volcanic rock horizons preserved in the Jebel Ank section, vanadium may be primarily associated with the process of goethite precipitation during the initial formation of the ironstones. The relatively high contents of V in the studied samples are probably due to the occurrence of V in the structure of goethite (e.g. Schwertmann and Pfab, 1997; Kaur et al., 2009). The affinity of Al^{3+}, V^{3+}, Cr^{3+}, Mn^{3+}, Mo^{3+}, U^{6+} and for Fe–oxyhydroxides is also well documented and manifests in different ways such as isomorphic substitutions (Fe^{3+} in the octahedral position) or surface adsorption (Cornell and Schwertmann, 2003). The lower contents of detrital-derived elements such as Y, Nb and Zr support the previous conclusion from the major oxide contents that the Jebel Ank area might have received minor detrital inputs during the iron deposition.

Hydrothermal Fe-Mn deposits show higher contents of Zn, Pb, Mo, V and As and are depleted in Co, Ni and Cu relative to hydrogenous deposits (Hewett et al., 1963; Nicholson, 1992; Boyd and Scott, 1999). In this regard, the Jebel Ank goethite show low Cu, Pb, As, and Zn contents and is enriched in Co, and Ni and this could suggest a hydrogenous source of the ore. The discrimination diagram based on Ni + Co *vs.* As + Cu + Mo + Pb + V + Zn of Nicholson (1992) also indicates that the Jebel Ank iron deposit displays hydrogenetic type mineralization (Fig. 12B).

The hydrogenous and hydrothermal deposits can be also distinguished by using Co/Ni and Co/Zn ratios (Toth, 1980). A ratio of Co/Ni < 1 and Co/Ni > 1 indicates a sedimentary origin and a deep marine environment, respectively (Delian, 1994; Fernandez and Moro, 1998; Öksüz, 2011). A ratio of Co/Zn of 0.15 is indicative of a hydrothermal type deposit and a ratio of 2.5 indicates a hydrogenous type deposit (Toth, 1980). In bulk samples and Fe-oolite, Co/Ni ratios range from 0.40 to 0.59 (average = 0.33). Co/Zn ratios range from 0.25 to 0.33 (average = 0.29). Although Co/Zn ratios point to a hydrothermal source for Fe mineralization, Co/Ni ratios of ore samples indicate that sedimentary environments played an important role during the formation of the Fe deposits through their plotting within the hydrogenetic field of the Zn–Ni–Co diagram of Choi and Hariya (1992) (Fig. 12C).

A positive Eu anomaly and low ∑REE (<100 ppm), are characteristics of hydrothermal deposits, while a positive Ce anomaly and high ∑REE are characteristics of hydrogenetic deposits (Usui et al., 1997; Bau et al., 2014). The total REE-Y contents of bulk sample and oolite are conformable with hydrogenous Fe-deposits (average = 446.9, Table 3). Fe-Mn oxyhydroxides have been considered by many authors as REE concentrators and it has been reported that extremely slow growth rates allow hydrogenous oxides to scavenge REEs for longer times from seawater (Surya Prakash et al., 2012).

Fig. 11B shows the REE-Y patterns of bulk samples and oolites compared with those of hydrothermal, hydrogenetic and diagenetic Fe-Mn precipitates (Bau et al., 2014). Results indicate HREE-enriched patterns with positive Ce and negative Y anomalies, which resemble the pattern of hydrogenous deposits from other parts of the world (Fig. 11B). The discrimination Ce/Ce∗ vs Nd and Ce/Ce∗ vs Y_N/Ho_N (Fig. 11C and D) diagrams of Bau et al. (2014) confirm the mostly hydrogenetic origin and suggest that there is no evidence of volcanic activity in the basin when these Fe-oolites formed. Further, the absence of volcanic material in the samples from this study also suggests a non-volcanic origin for the Fe-oolites. La/Ce ratios in the studied goethite vary between 0.11 and 0.17 (average 0.14), which is very close to hydrogenous Mn-Fe crusts (0.25, Nath et al., 1997). Goethite in the Jebel Ank

deposit is purely hydrogenous and has received major contributions from seawater.

The most probable source of Fe is from rocks that were exposed at surface during Eocene time, and were subjected to chemical weathering and erosion under a humid, tropical climate. These products, dominated by amorphous Fe-oxyhydroxides, clays, and quartz, were transported by rivers and deposited in fluviatile and lacustrine environments located in the Jebel Ank area. Solignac (1930) reported that the oolitic layer pinchs out laterally to a glauconite rich-sandstone layer. Submarine weathering of glauconite could enhance dissolved Fe concentration in the seawater during the formation of the Jebel Ank ore. This scenario was recently considered for the Middle Eocene Bahariya iron ores in Egypt (Baioumy et al., 2014). A continental origin for the iron from weathering of adjacent areas can also be envisaged given the higher phosphorus and zinc concentrations. The specific source area for the oolitic iron is uncertain, but may lie somewhere to the east, because as M'hamdi (1984) stated, the sandstone footwall level was separated from a shoreline to the west by the laterally equivalent deeper water clays. The provenance of the large amount of iron in the Jebel Ank oolitic ironstones remains unresolved. However, a continental sedimentary source is most plausible.

There are many similarities between the Jebel Ank oolitic ironstones and Tertiary ironstone deposits in Egypt studied by Salama et al. (2012, 2014) and Baioumy et al. (2014, 2017). Similarities include: (i) lagoonal-shallow intertidal depositional environments; (ii) deposition during transgression–regression events; mineral assemblages (goethite, apatite, quartz, various Mn-bearing minerals, Fe-sulfate minerals and clay minerals); (iii) oolitic texture formed as direct precipitation of Fe-rich minerals on suspended nuclei; (iv) Fe and Mn fractionation producing high Fe/Mn ratios causing Fe precipitation in the upper part of the succession and Mn in the lower part; (v) high V, Zn, Mo contents; and (vi) the lateritic materials produced by the weathering of the adjacent continental masses, which are considered to be the main source of iron.

In addition to the age difference, dissimilarities between the Jebel Ank oolitic ironstones and Tertiary ironstone deposits in Egypt include: (i) consistency in lateral and vertical facies and homogenous composition. absence of marine fauna, microorganisms, ferruginized clasts and/or fossil, sedimentary features, and particle size sorting in Jebel Ank deposit; (ii) different ironstone facies, paragenesis, and depositional stages controlled by variations in pH–Eh, biological activities and climatic conditions; mixed hydrothermal and hydrogenous sources of the iron ore deposits in Egypt.

6. Conclusions

The Late Eocene Jebel Ank oolitic ironstone deposit is composed of goethite-oolites and reduced detrital non-ferruginous gangue deposited in a near-shore shallow marine environment. The thickness of the oolitic iron layer is variable, ranging from a few centimeters to 8 m thick. The ironstone layer shows good vertical continuity and mineralogical and geochemical consistency. Field and petrographic investigations indicate that Fe-oolites are of primary depositional origin. XRD, spectroscopic and mineral chemical analyses show low to negligible Al-Fe substitution in the goethite structure, which rules out any replacement of a precursor mineral by goethite. The enriched V, Cr, Ni, Zn, and REE-Y contents are controlled by adsorption on goethite. Trace elements and REE discrimination diagrams show evidence of a hydrogenous origin. PAAS-normalized REE-Y patterns, positive Ce and negative Y anomalies indicate oxic conditions. Fe enrichment in seawater could be due the weathering of adjacent continental hinterland.

Acknowledgements

The authors thank Dr. Donatella Barca and Mariano Davolli from Università della Calabria (Italy) for LA-ICP-MS and SEM analyses. We also thank Dr. Sheldon Skaggs from Bronx Community College, CUNY (USA) for clarification of the translation into English. Sophie Decree and Faraj Tobia are thanked for reviewing the manuscript and their extremely helpful comments and annotations. We are grateful to Associate Editor Paul During for his contributions to increase the quality of our paper.

References

Adeleye, D.R., 1975. Derivation of fragmentary oolites and pisolites from dessication cracks. J. Sediment. Petrol. 45, 794–798.
Adler, H.H., Kerr, P.F., 1965. Variations in infrared spectra, molecular symmetry, and site symmetry of sulfate minerals. Am. Mineral. 50, 132–147.
Ahmadi, R., Mercier, E., Ouali, J., 2013. Growth-strata geometry in fault-propagation folds: a case study from the Gafsa basin, southern Tunisian Atlas. Swiss J. Geosci. 106, 91107.
Ben Haj Ali, M., Jedoui, Y., Dali, T., Ben Salem, H., Memmi, L., 1985. Carte géologique de la Tunisie au 1/500 000. Edt. Service Géologique. Office National des Mines.
Baioumy, H.M., Khedr, M.Z., Ahmed, A.H., 2013. Mineralogy, geochemistry and origin of Mn in the high-Mn iron ores, Bahariya Oasis, Egypt. Ore. Geol. Rev. 53, 63–76.
Baioumy, H.M., Ahmed, A.H., Khedr, M.Z., 2014. A mixed hydrogenous and hydrothermal origin of the Bahariya iron ores, Egypt: evidences from the trace and rare earth element geochemistry. J. Geochem. Explor. 146, 149–162.
Baioumy, H., Omran, M., Fabritius, T., 2017. Mineralogy, geochemistry and the origin of high-phosphorus oolitic iron ores of Aswan, Egypt. Ore. Geol. Rev. 80, 185–199.
Bau, M., Koschinsky, A., Dulski, P., Hein, J.R., 1996. Comparison of the partitioningbehaviours of yttrium, rare earth elements, and titanium between hydrogeneticmarine ferromanganese crusts and seawater. Geochim. Cosmochim. Acta 60, 1709–1725.
Bau, M., Schmidt, K., Koschinsky, A., Hein, J., Kuhn, T., Usui, A., 2014. Discriminating between different genetic types of marine ferro-manganese crusts and nodules based on rare earth elements and yttrium. Chem. Geol. 381, 1–9.
Bayer, U., 1989. Stratigraphic and environmental patterns of ironstone deposits. In: Young, T.P., Taylor, W.E.G. (Eds.), Phanerozoic Ironstones, vol. 46. Geol. Soc. Spec. Publ., pp. 105–117.
Ben Ayed, N., 1993. Evolution Tectonique De L'avant-Pays De La Chaîne Alpine De La Tunisie Du Début Du Mésozoïque À l'Actuel Thèse es-sciences. Univ. Paris Sud, Orsay, p. 347.
Bensalem, M.S., Ghanmi, M., Zargouni, F., 2010. Genesis of folds in external zone: application of fault propagation fold. Gafsa basin example (southern central Tunisia). Arab. J. Geosci. 4, 229–237.
Berthon, L., 1922. L'industrie minérale de la Tunisie. Tunis, 272p.
Bhattacharya, D.P., Kakimoto, P., 1982. Origin of ferriferous ooids: an SEM study of ironstone ooids and bauxite pisoids. J. Sed. Petrol. 52, 849–857.
Bishop, J.L., Murad, E., 2005. The visible and infrared spectral properties of jarosite and alunite. Am. Mineral. 90, 1100–1107.
Bouaziz, S., Barrier, E., Soussi, M.M., Turki, M.M., Zouari, H., 2002. Tectonic evolution of the northern African margin in Tunisia from paleostress data and sedimentary record. Tectonophysics 357, 227–253.
Boukadi, N., 1985. Evolution géodynamique et cinématique de la zone d'interférence de l'axe Nord-Sud et de la chaîne de Gafsa (Maknassy-Mezzouna et Jebel Bouhedma) Thèse Doct. 3ème cycle. Univ. Strasbourg, France, p. 143.
Boukadi, N., 1994. Structuration de l'Atlas de Tunisie. Signification géométrique et cinématique des nœuds et des zones d'interférences structurales au contact de grands couloirs tectoniques Thèse ès Sciences. Univ. Tunis II, Tunisia. 249p.
Boyd, T., Scott, S.D., 1999. Two-XRD-line ferrihydrite and Fe–Si–Mn oxyhydroxide mineralization from Franklin Seamount, western Woodlark Basin, Papua New Guinea. Can. Mineral. 37, 973–990.
Braun, J.J., Pagel, M., Muller, J.P., Bilong, P., Michard, A., Guillet, B., 1990. Cerium anomalies in lateritic profiles. Geochim. Cosmochim. Acta 54, 781–795.
Burkhalter, R.M., 1995. Ooidal ironstones and ferruginous microbialites: origin and relation to sequence stratigraphy (Aalenian and Bajocian, Swiss Jura mountains). Sedimentology 42, 57–74.
Burollet, P.F., 1956. Contribution à l'étude stratigraphique de la Tunisie Centrale. Annales des mines et de la géologie 18, 345.
Burollet, P.F., Oudin, J. P., 1980. Paléocène et Eocène en Tunisie – Pétrole et phosphate, Géologie Comparée des Gisements de Phosphate et de Pétrole. BRGM, Orléans, pp. 205–216.
Cambier, P., 1986. Infrared study of goethites of varying crystallinity and particle size: I. Interpretation of OH and lattice frequencies. Clay Miner. 21, 191–200.
Canavan, R.W., Van Cappellen, P., Zwolsman, J.J.G., van den Berg, G.A., Slomp, C.P., 2007. Geochemistry of trace metals in a fresh water sediment: field results and diagenetic modelling. Sci. Total Environ. 381, 263–279.
Cayeux, L., 1909. Les minerals de fer oolithiques de France. Tome 1: Minerais de fer primaires. Imprimerie Nationale, Paris.

Chaabani, F., 1995. Dynamique De La Partie Orientale Du Bassin De Gafsa Au Crétacé Et auPaléogène: Etude Minéralogique Et Géochimique De La Série Phosphatée Eocène, Tunisie méridionale Thèse Doctrat d' Etat. Université de Tunis II, Tunis.
Champetier, Y., Hambadou, E., Hambodou, H., 1987. Examples of biogenic support of mineralisation in two oolitic iron oresLorraine (France) and Gara Djebilet (Algeria). Sediment. Geol. 51, 249255.
Chauvel, J.J., 1968. Contribution À L'étude Des Gisements De Fer De l'Ordovicien Inférieur De Bretagne Thèse de doctorat Dr. ès-Sci. Nat.. Université de Rennes, Rennes, France.
Chauvel, J.J., 1974. Les minerais de fer de l'Ordovicien inferieur du bassin de Bretagne, Anjou, France. Sedimentology 21, 127–147.
Choi, J.H., Hariya, Y., 1992. Geochemistry and depositional environment of Mn Oxide deposits in the Tokoro Belt, Northeastern Hokkaido. Econ. Geol. 87, 1265–1274.
Chukanov, N.V., 2014. Infrared Spectra of Mineral Species: Extended Library. Springer-Verlag GmbH, Dordrecht-Heidelberg-New York-London. 1716p.
Ciobotă, V., Salama, W., Tarcea, N., Rösch, P., El Aref, M., Gaupp, R., Popp, J., 2012. Identification of minerals and organic materials in Middle Eocene ironstones from the Bahariya Depression in the Western Desert of Egypt by means of micro-Raman spectroscopy. J. Raman Spectrosc. 43, 405–410.
Collin, P.Y., Loreau, J.P., Courville, P., 2005. Depositional environments and iron ooid formation incondensed sections (Callovian–Oxfordian, south-eastern Paris basin, France). Sedimentology 52, 969–985.
Cornell, R.M., Schwertmann, U., 2003. The Iron Oxides: Structure, Properties, Reactions, Occurrences and Uses. Wiley-VCH, Weinheim, p. 664p.
Cotter, E., 1992. Diagenetic alteration of chamositic clay minerals to hematite in oolitic ironstone. J. Sed. Petrol. 62, 54–60.
Dahanayake, K., Krumbein, W.E., 1986. Microbial structures in ooidal iron formations. Miner. Deposita 21, 85–94.
de Faria, D.L.A., Venâncio Silva, S., de Oliveira, M.T., 1997. Raman microspectroscopy of some iron oxides and oxyhydroxides. J. Raman Spectrosc. 28, 873–878.
Delian, F., 1994. Geological and Geochemical Research of the Manganese Ore Bed (in Chinese), M1. Weather Publishing Press, Beijing.
Dercourt, J., Zonenshain, L.P., Ricou, L.P., Kazmin, V.G., Le Pichon, X., Knipper, A.L., Laurier, J.P., Bashenov, M.L., Boulin, J., Pechersky, D.H., Biju Duval, B., Savostin, L. A., Lepvrier, C., Geyssant, J., 1986. Geological evolution of the Tethys belt from the Atlantic to the Pamirs since the LIAS. Tectonophysics 123 (1–4), 241–315.
Donaldson, W.S., Olint, A.G., Longstaffe, F.J., 1999. Tectonic and eustatic control on deposition and preservation of upper Cretaceous ooidal ironstone and associated facies. Sedimentology 46, 1159–1182.
Drouet, C., Navrotsky, A., 2003. Synthesis, characterization and thermochemistry of K-Na–H3O jarosites. Geochim. Cosmochim. Acta 67, 2063–2076.
Fernandez, A., Moro, M.C., 1998. Origin and depositional environment of Ordovician stratiform iron mineralization from Zamora (NW Iberian Peninsula). Miner. Deposita 33, 606–619.
Fitzpatrick, R.W., Schwertmann, U., 1982. Al-substituted goethite. An indicator of pedogenetic and other weathering environments in South Africa. Geoderma 27, 335347.
Francesco, A.M.D., Bocci, M., Crisci, G.M., Lanzafame, U., 2005. Carratteriz-zazione archeometrica della ossidiane del M.Arci: confronto fra metodologia tradizionale in XRF e metodologia XRF non distruttiva, Atti del III Convegno Iternazionale "L'ossidiana del Monte Arci nel Meditterraneo". Pau (OR) Ed.PTM (OR), pp. 117–128.
Fryer, B.J., Jackson, S.E., Longerich, H.P., 1995. The design, operation and role of the laser-ablation microprobe coupled with an inductively coupled plasma-mass spectrometer (LAM-ICP-MS) in the earth Sciences. Can. Mineral. 33, 303–312.
Gaied, M.E., Chaabani, F., Gallala, W., 2015. Alunite characterization in the upper Eocene clay deposits of Central Tunisia: an implication to its genesis. Carbonates Evaporites 30, 347–356.
Gao, S., Liu, X., Yuan, H., Hattendorf, B., Gunther, D., Chen, L., Hu, S., 2002. Determination of forty-two major and trace elements in USGS and NIST SRM glasses by laser ablation-inductively coupled plasma-mass spectrometry. Geostandards Newsl. J. Geostand. Geoanal. 26 (2), 181–196.
Garnit, H., Bouhlel, S., Barca, D., Chtara, C., 2012. Application of LA-ICP-MS tosedimentary phosphatic particles from Tunisian phosphorite deposits: Insights from trace elements and REE into paleo-depositional environments. Chem. Erde-Geochem. 72, 127–139.
Gehring, A.U., 1989. The formation of goethitic ooids in condensed deposits in northern Switzerland. In: Young, T.P., Taylor, W.E.G. (Eds.), Phanerozoic Ironstones, vol. 46. Geol. Soc. Spec. Publ., pp. 133–139.
Gharbi, M., Espurt, N., Masrouhi, A., Bellier, O., Amari, E.A., 2015. Style of Atlassic tectonic deformation and geodynamic evolution of the southern Tethyan margin, Tunisia. Mar. Pet. Geol. 66, 801816.
Gottis, C., Sainfeld, P., 1952. Les gîtes métallifères tunisiens. XIX Congrès Géolo. Int. Monographies régionales, 2ème série, Tunisie, 2, 104p.
Harder, H., 1989. Mineral genesis in ironstones: a model based upon laboratory experiments and petrographic observations. In: Young, T.P., Taylor, W.E.G. (Eds.), Phanerozoic Ironstones, vol. 46. Geol. Soc. Spec. Publ., pp. 9–18.
Hem, J.D., Cropper, W.H., 1959. Chemistry of iron in natural water – a survey of ferrous-ferric chemical equilibria and redox potentials. U.S. Geol. Survey Water-Supply Paper 1459-A, 31.
Hemingway, J.E., 1974. Jurassic. In: Raynor, D.H., Hemingway, J.E. (Eds.), The Geology and Mineral Resources of Yorkshire. Yorkshire Geological Society, pp. 161–223.
Hewett, D.F., Fleischer, M., Conklin, N., 1963. Deposits of the manganese oxides: supplement. Econ. Geol. 58, 1–51.
Hlaiem, A., 1999. Halokinesis and structural evolution of the major features in eastern and southern Tunisian Atlas. Tectonophysics 306, 79–95.
James, H.L., 1966. Chemistry of the iron-rich sedimentary rocks. U.S. Geological Survey Professional Papers 440-W1-W61.
Kaur, N., Singh, B., Kennedy, B.J., Grafe, M., 2009. The preparation and characterization of vanadium substituted goethite: the importance of temperature. Geochim. Cosmohim. Acta 73, 582–593.
Kennedy, B.A., 1990. Surface Mining, Society for Mining, Metallurgy and Exploration Inc. second ed. Port City Press, Baltimore, Maryland, pp. 48–60.
Khan, R.M.K., Naqvi, S.M., 1996. Geology, geochemistry and genesis of BIF of Kushtagi schist belt, Archaean Dharwar Craton, India. Miner. Deposita 31 (1), 123–133.
Kimberley, M.M., 1979. Origin of oolitic iron formations. J. Sed. Petrol. 49, 111–132.
Kubisz, J., 1972. Studies on synthetic alkali-hydronium jarosites. III. Infrared absorption study. Mineral. Polonica 3, 23–35.
Liu, H., Chen, T., Zou, X., Qing, C., Frost, R.L., 2013. Effect of Al content on the structure of Al-substituted goethite: a micro-Raman spectroscopic study. J. Raman Spectrosc. 44, 1609–1614.
M'hamdi, S., 1984. Le gisement de fer oolithique du J'bel Ank, Tunisie méridionale. Etude sédimentologique et géochimique Thèse de spécialité 3ème cycle. Université Louis Pasteur. 125p.
Macquaker, J.H.S., Taylor, K.G., Young, T.P., Curtis, C.D., 1996. Sedimentological and geochemical controls on ooidal ironstone and "bone-bed" formation and some comments on their sequence stratigraphical significance. In: Hesselbo, S., Parkinson, D.N. (Eds.), Sequence Stratigraphy in British Geology, vol. 103. Geol. Soc. Spec. Publ., pp. 97–107.
Maynard, J.B., 1986. Geochemistry of oolitic iron ore, an electron microprobe study. Econ. Geol. 81, 1473–1483.
Maynard, J.B., Van Houten, F.B., 1992. Descriptive model of oolitic ironstones. In: Bliss, J.D. (Ed.), Developments in mineral deposit modeling. U.S. Geological Survey Bulletin, pp. 39–40.
McLennan, S.M., 1989. Rare earth elements in sedimentary rocks: influence of provenanceand sedimentary processes. In: Lipin, B.R., McKay, G.A. (Eds.), Geochemistry and Mineralogy of Rare Earth Elements. Mineral. Soc. Am., pp. 169–200.
Mesaed, A.A., 2004. Mechanism of formation of the Upper Eocene Glauconitic Ironstones and Red Beds of Gabal Qalamoon area, Western Desert, Egypt. Egypt J. Geol. 48, 17–44.
Mesaed, A.A., Harbi, R.T.H., 2013. Stratigraphic setting, facies types, depositional environments and mechanism of formation of Ash Shumaysi ironstones, Wadi Ash Shumaysi, Jeddah district, West Central Saudi Arabia. Arab. J. Geosci. 6, 213–233.
Millot, G., 1964. Géologie des argiles. Masson et Cie Ed., 499 p.
Murphy, P.J., Smith, A.M.L., Hudson-Edwards, K.A., Dubbin, W.E., Wright, K., 2009. Raman and IR spectroscopic studies of aluntie-supergroup compounds containing Al, Cr^{3+}, Fe^{3+} and V^{3+} at the *B* site. Can. Mineral. 47, 663681.
Mutrux, J., Maher, H., Shuster, R., Hays, T., 2008. Iron ooid beds of the Carolinefjellet Formation, Spitsbergen, Norway. Polar Res. 27, 28–43.
Nath, B.B., Pluger, W.L., Roelandts, I., 1997. Geochemical constraints on thehydrothermal origin of ferromanganese incrustations from the Rodriguez triple junction, Indian Ocean. In: Nicholson, K., Hein, J.R., Bühn, B., Dasgupta, S. (Eds.), Manganese Mineralization: Geochemistry and Mineralogy of Terrestrial and Marine Deposits, vol. 119. Geol. Soci. Lond. Spec. Publ., pp. 199–211.
Nicholson, K., 1992. Contrasting mineralogical–geochemical signatures of manganese oxides: guides to metallogenesis. Econ. Geol. 87, 1253–1264.
Nicolini, P., 1967. Remarques comparatives sur quelques éléments sédimentologiques et paléogéographiques liés aux gisements de fer de Djebel Ank (Tunisie) et de Lorraine (France). Miner. Deposita 2, 95–101.
Öksüz, N., 2011. Geochemical characteristics of the Eymir (Sorgun-Yozgat) manganese deposits, Turkey. J. Rare. Earths 29 (3), 287–296.
Olsen, R.A., Eccles, D.R., Collom, C.J., 1999. A study of potential co-product trace elements within the clear hills iron deposits, Northwestern Alberta. AGS/AEUB Special Report 08, 190p.
Pearce, N.J.G., Perkins, W.T., Westgate, J.A., Gorton, M.P., Jackson, S.E., Neal, C.R., Chenery, S.P., 1997. A compilation of new and published major and trace data for NIST SRM 610 and NIST SRM 612 glass reference materials. Geostandards Newsl. J. Geostand. Geoanal. 21 (1), 115–144.
Pedersen, T.F., Price, N.B., 1982. The geology of manganese carbonate in Panama Basin sediments. Geochim. Cosmochim. Acta 46, 59–68.
Petránek, J., Van Houten, F.B., 1997. Phanerozoic ooidal ironstones. Czech Geol. Surv., Special paper 7, 71.
Price, N.B., 1976. Chemical diagenesis in sediments. In: Riley, J.P., Chester, R. (Eds.), Chemical Oceanography, vol. 6. Acad. Press, Inc, United States (USA).
Said, A., Dominique, C., Baby, P., Ouali, J., 2011. Active oblique ramp faulting in the Southern Tunisian Atlas. Tectonophysics 499, 178189.
Salama, W., El Aref, M.M., Gaupp, R., 2012. Mineralogical and geochemical investigations of the Middle Eocene ironstones, El Bahariya Depression, Western Desert, Egypt. Gondwana Res. 22, 717–736.
Salama, W., El Aref, M.M., Gaupp, R., 2013. Mineral evolution and processes of ferruginous microbialite accretion – an example from the Middle Eocene stromatolitic and ooidal ironstones of the Bahariya Depression, Western Desert, Egypt. Geobiology 11, 15–28.
Salama, W., El Aref, M., Gaupp, R., 2014. Facies analysis and palaeoclimatic significance of ironstones formed during the Eocene greenhouse. Sedimentology 61, 1594–1624.

Salama, W., El Aref, M., Gaupp, R., 2015. Spectroscopic characterization of iron ores formed in different geological environments using FTIR, XPS, Mössbauer spectroscopy and thermoanalyses. Spectrochim. Acta Mol. Biomol. Spectrosc. 136, 1816–1826.
Sassi, S., 1974. La Sédimentation Phosphatée Au Paléocène Dans Le Sud Et Le Centre Ouest De La Tunisie Thèse Doct. ès-Sci.. Univ. Paris Sud Orsay, France.
Schulze, D.G., 1984. The influence of aluminum on iron-oxides. 8: Unit cell dimensions of Al-substituted goethites and estimation of Al from them. Clays Clay Miner. 32, 36–44.
Schulze, D.G., Schwertmann, U., 1984. The influence of aluminium on iron oxides. X: Properties of A1-substituted goethites. Clay Miner. 19, 521–539.
Schwertmann, U., Pfab, G., 1997. Structural vanadium and chromium in lateritic iron oxides: genetic implications. Geochim. Cosmochim. Acta 60, 4279–4283.
Serna, C.J., Cortina, C.P., Ramos, J.V.G., 1986. Infrared and Raman study of alunite–jarosite compounds. Spectrochim. Acta 42A, 729–734.
Shields, G., Stille, P., 2001. Diagenetic constraints on the use of cerium anomalies aspalaeoseawater redox proxies: an isotopic and REE study of Cambrian phosphorites. Chem. Geol. 175, 29–48.
Siehl, A., Thein, J., 1989. Minette-type ironstones. In: Phanerozoic Ironstones. In: Young, T.P., Taylor, W.E.G. (Eds.), vol. 46. Geol. Soc. Spec. Publ., pp. 175–193.
Solignac, M., 1930. Les caractères minéralogiques du minerai de fer oolithique du Jebel Ank (Tunisie méridionale). C.R. Aad. Sci. Paris 191, 107–109.
Sorby, H.C., 1856. On the origin of the Cleveland Hill Ironstone. Proceedings of the Geological and Polytechnic Society of the West Riding of Yorkshire, 3, 457–461.
Stucki, J.W., Goodman, B.A., Schwertmann, U. (Eds.), 1988. Iron in Soils and Clay Minerals. D. Reidel, Dordrecht. 893.
Sturesson, U., 2003. Lower Paleozoic iron oolites and volcanism from a Baltoscandian perspective. Sediment. Geol. 159, 241–256.
Surya Prakash, L., Ray, D., Paropkari, A.L., Mudholkar, A.V., Satyanarayanan, M., Sreenivas, B., Chandrasekharam, D., Kota, D., Raju, K.A.K., Kaisary, S., Balaram, V., Gurav, T., 2012. Distribution of REEs and yttrium among major geochemical phases of marine Fe–Mn-oxides: comparative study between hydrogenous and hydrothermal deposits. Chem. Geol. 312–313, 127–137.
Swayze G.A., Desborough G.A., Smith K.S., Lowers H.A., Hammarstrom J.M., Diehl S. F., Leinz R.W., Driscoll R.L., 2008. Understanding jarosite – from mine waste to Mars. In Characteristics of some natural jarosites 1055 Understanding Contaminants Associated with Mineral Deposits (ed. P. L. Verplanck). USGS Circular. 1328, pp. 8–13.
Taylor, S.R., McLennan, S.M., 1985. The Continental Crust: Its Composition and Evolution. Blackwell Scientific Publications, London, pp. 42–52.
Tobia, F.H., Kettanah, Y.A., Mustafa, M.M., 2014. Petrography and geochemistry of Ga'ara sedimentary ironstones, Western Desert of Iraq. J. Afr. Earth Sci. 97, 261–272.
Toth, J.R., 1980. Deposition of submarine crusts rich in manganese and iron. Bull. Geol. Soc. Am. 91, 44–54.
Usui, A., Bau, M., Yamazaki, T., 1997. Manganese microchimneys buried in the Central Pacific pelagic sediments: evidence of intraplate water circulation? Mar. Geol. 141, 269–285.
Van Houten, F.B., 1992. Review of Cenozoic ooidal ironstones. Sed. Geol. 78, 101–110.
Van Houten, F.B., Arthur, M.A., 1989. Temporal patterns among Phanerozoic oolitic ironstones and oceanic anoxia. In: Young, T.P., Taylor, W.E.G. (Eds.), Phanerozoic Ironstones: An Introduction and Review. Geological Society of London, London, pp. 33–49.
Van Houten, F.B., Purucker, M.E., 1984. Glauconitic peloids and chamositic ooids – favourable factors, constraints and problems. Earth Sci. Rev. 20, 211–243.
Winnock, E., 1980. Les dépôts de l'Eocene au Nord de l'Afrique: aperçu paléogéographique de l'ensemble. In: Géologie Comparée des Gisements de Phosphates et de Pétrole. BRGM, Orléans, pp. 219–243.
Wronkiewicz, D.J., Condie, K.C., 1987. Geochemistry of Archean shales from the Witwatersrand Supergroup, South Africa: Sourcearea weathering and provenance. Geochim. Cosmochim. Acta 51, 24012416.
Young, T.P., 1989a. Phanerozoic ironstones: an introduction and review. In: Young, T.P., Taylor, W.E.G. (Eds.), Phanerozoic Ironstones, vol. 46. Geol. Soc. Spec. Publ., pp. 9–25.
Young, T.P., 1989b. Eustatically controlled ooidal ironstone deposition: facies relationships of the Ordovician openshelf ironstones of Western Europe. In: Young, T.P., Taylor, W.E.G. (Eds.), Phanerozoic Ironstones, vol. 46. Geol. Soc. Spec. Publ., pp. 51–63.
Zaïer, A., Béji-Sassi, A., Sassi, S., Moody, R.T.J., 1998. Basin evolution and deposition during the Early Paleocene in Tunisia. In: Macgregor, D.S., Moody, R.T.J., Clark-Lowes, D.D. (Eds.), Petroleum Geology of North Africa, vol. 132. Geol. Soc. London Spec. Publ., pp. 375–393.
Zargouni, F., 1985. Tectonique de l'Atlas méridional de Tunisie, évolution géométrique et cinématique des structures en zone de cisaillement Thèse d'Etat. Univ. Louis Pasteur, Strasbourg-Paris.
Zargouni, F., Rabiaa, M.C., Abbés, C., 1985. Rôle des couloirs de cisaillement de Gafsa et de Négrine-Tozeur dans la structuration du faisceau des plis des Chotts, éléments de l'accident sud-atlasique. CR Acad. Sci. Paris 301 (11), 831–883.
Zouaghi, T., Bédir, M., Inoubli, M.H., 2005. Structuration profonde des dépôts de l'Albien–Maastrichtien en Tunisie centrale: nouvelle limite de l'archipel de Kasserine et implications géodynamiques. C.R. Géosci. 337, 685–693.
Zouaghi, T., Ferhi, I., Bédir, M., Ben Youssef, M., Gasmi, M., Inoubli, M.H., 2011. Analysis of Cretaceous (Aptian) strata in central Tunisia, using 2D seismic data and well logs. Afr. Earth Sci. 61, 38–61.
Zouari, H., Turki, M.M., Delteil, J., 1990. Nouvelles données sur l'évolution tectonique de la chaîne de Gafsa. Bull. Soc. Géol. France 8, 621–628.